RESEARCH

Anti-interrupted-sampling repeater jamming method based on frequency agility waveform and sparse recovery

Yunhao Ji[1], Shan Wei[1*] and Yaobing Lu[1]

*Correspondence:
wishan@stu.cpu.edu.cn

[1] Beijing Institute of Radio Measurement, China Aerospace Science and Industry Corp Second Research Institute, Beijing 100854, China

Abstract

Interrupted-sampling repeater jamming (ISRJ) is a type of intra-pulse coherent jamming that poses a significant threat to radar detection and tracking of targets. This paper proposes an ISRJ suppression method based on frequency agile waveform and sparse recovery, starting from the temporal discontinuity and modulation characteristics of ISRJ. This method is particularly suitable for scenarios with high jamming duty ratio (JDR) and high jammer sampling duty ratio (SDR). By dividing the transmitted waveform into sub-pulses with different carrier frequencies and applying a two-round block sparse algorithm, the method accurately recovers three parameters of ISRJ, achieving effective jamming identification, reconstruction, and cancellation. Additionally, a target detection technique based on robust sparse recovery is proposed, significantly improving the stability and accuracy of target detection. Comparative experimental results conducted in three scenarios confirm the effectiveness and superiority of this method under high JDR and SDR conditions.

Keywords: Electronic warfare, Radar signal processing, Radar anti-jamming

1 Introduction

In modern electronic warfare, radar's anti-jamming ability plays a pivotal role in determining combat effectiveness and achieving information superiority [1–3]. Digital radio frequency memory (DRFM) technology allows jammers to accurately intercept and replicate radar signals quickly. In intermittent sampling storage mode, DRFM can repeatedly transmit jamming slices within the current pulse repetition period (PRI), creating intra-pulse coherent interrupted-sampling repeater jamming. Leveraging the coherence characteristics of pulse compression (PC) radar and the high Doppler tolerance of wideband signals, ISRJ appears as a false target cluster on the range profile, with a primary false target and symmetric secondary ones, achieving both blanket and deceptive jamming effects [4, 5]. Currently, ISRJ is widely employed in electronic countermeasures. Compared with traditional jamming, ISRJ is more difficult to counter with current methods like intra-pulse waveform agility [6, 7] and multi-carrier frequency phase encoding [8] than traditional jamming, highlights the need to research and develop of effective anti-jamming strategies.

Ji *et al. EURASIP Journal on Advances in Signal Processing*　　(2024) 2024:55

Page 2 of 34

To address the challenges posed by ISRJ, scholars have developed a series of counter-measures. Due to the flexibility and diversity of ISRJ, there is currently no unified classification method for these measures. However, they can generally be divided into two main categories: active counter-strategies and passive counter-strategies. The passive strategies focus on signal processing at the receiver end. Within this category, time–frequency (TF) analysis stands out as an effective method. It helps distinguish the target signals from ISRJ by analyzing their differences in the time and frequency domains. Chen et al. analyzed the time–frequency characteristics of the target echo after stretching, introducing the max-TF function for jamming-free period extraction and a smoothing filter for jamming elimination [9]. Wei et al. proposed an efficient filter for extended targets based on time–frequency analysis for ISRJ suppression [10]. Based on the concept of reconstruction-cancellation, Zhou et al. used TF analysis to estimate jamming slices number and forwarding times, allowing iterative jamming component cancellation [11]. Meng et al. used TF analysis and Hilbert transform to estimate sampling pulse width and intervals, further calculating sampling and forwarding times [12]. Chen et al. applied TF analysis to distributed radar systems, identifying jamming and extracting data for adaptive beamformer training. [13]. The TF analysis method's limitation emerges under high jamming duty ratio. In this case, obtaining jamming-free periods proves to be particularly challenging, leading to a substantial decrease in the accuracy of jamming parameter estimation. While collaborative spatial processing can mitigate the effects of high JDR to some extent, the deployment of a distributed radar system necessitates additional resources. Based on time–frequency analysis, several derivative signal processing methods have been developed to counter ISRJ. Han et al. first used short-time fractional Fourier transform to initially locate the jamming fragments, further refined the jamming edges through differential filtering and deconvolution, thus improving the parameter estimation accuracy [14]. Yuan et al. designed the energy function to detect the jamming-free period, and used a specific filtering method to suppress ISRJ [15]. However, the performance of the two methods significantly decreases with weaker jamming intensity. Chen et al. designed a neural network filtering method to improve the extraction accuracy of jamming-free periods [16]. However, this method cannot cope with high JDR situations. Wu et al. developed an efficient ISRJ identification method based on integral decomposition [17], focusing on energy distribution differences. While successful in real-time radar applications, its effectiveness against strong jamming is constrained by its post-CFAR implementation.

Active anti-jamming strategies that combine waveform design and signal processing show great promise. Shen et al. compared ISRJ performance of different waveforms, showing stepped frequency and linear frequency modulation waveforms yield similar jamming, while random frequency waveforms, in direct forwarding, create only one false target, with effectiveness declining with more sub-pulses [18]. Dai et al. analyzed down-chirp and up-chirp's quasi-orthogonal properties to design an orthogonal waveform, identifying ISRJ false targets by comparing peak positions [19]. However, this is effective only in direct forwarding. Zhou et al. developed a phase coding-based adaptive transmission scheme that dynamically suppresses ISRJ by estimating jammer position and duration with jamming perception, and optimizing the waveform using a genetic algorithm [20]. Liu et al. designed an intra-pulse agile waveform to enhance the

distinction between ISRJ and targets, combining fractional Fourier transform and filter design to suppress ISRJ [21]. However, the above four methods are less effective under intense jamming conditions. Zhang et al. utilized segmented LFM pulse orthogonality to achieve the sorting of jamming and targets [22]. They further designed an LFM waveform with intra-pulse Costa frequency stepped, which effectively reduced the jamming bands and jamming harmonics caused by segmented pulse compression [23]. However, this method cannot cope with the high SDR of the jammer. In summary, although various strategies have achieved certain results against ISRJ, each has limitations and specific application scenarios. Most methods recognize targets and ISRJ primarily in the time–frequency domain, which is a limited approach. This is particularly evident when the target and ISRJ overlap in the time domain, as the inability to discern target periods covered by jamming based solely on TF information forces the discarding of target echo segments contaminated by jamming. This significantly reduces the processing gain of subsequent PC for target identification, leading to poor performance in subsequent target recognition and jamming suppression stages. Especially in scenarios with high JDR and high jammer SDR, these methods suffer from a more severe decline in performance. Therefore, it is necessary to explore more efficient and robust strategies to effectively counter ISRJ.

In recent years, some scholars have successfully applied sparse recovery algorithms for anti-jamming and target identification, making some progress [24–27]. The central premise is that, even within complex electromagnetic environments, target signals can be accurately or approximately represented in specific transform domain with minimal basis vectors. Radar systems can detect the sparsity characteristics of these signals in the transform domain, enabling the effective separation of the target from jamming signals, ensuring stable target detection and tracking. However, current anti-jamming approaches based on sparse recovery still face challenges. The low signal-to-noise ratio (SNR) before PC complicates the stable recovery of target parameters. Furthermore, while designing dictionary matrices, most methods primarily focus on the waveform of real target, often simplistically treating the jamming slice as target echo with short pulse width. This approach overlooks the incompleteness of the ISRJ waveform caused by interrupted sampling in DRFM. Such an oversight can led to difficulties in accurately representing jamming echo sparsely, especially when the number of jamming slices is excessive, rendering the initial assumptions of sparsity no longer valid [28]. Moreover, few techniques consider designing radar transmission waveform at the transmission end, leading to dictionary matrices that often do not satisfy the restricted isometry property (RIP) [29], compromising the stability of sparse recovery.

To this end, this paper proposes an ISRJ suppression method with intra-pulse frequency agility, based on sparse recovery. Given that the intensity of ISRJ in actual scenarios is usually higher than that of real targets, the recoverability of ISRJ in sparse domains is more stable. Therefore, our work focuses on accurate recovery of jamming parameters. The method includes the following steps: First, divide the transmit pulse into multiple sub-pulses, and destroy the correlation between each sub-pulse through carrier frequency agility. This involves designing a dictionary matrix that satisfies the RIP, enabling effective sparse representation of both the target and ISRJ. Secondly, the received data undergo a sparse representation of delay-frequency to extract the modulation delay

and frequency information from the DRFM. Based on this information, the block delay-slicing dictionary is designed and updated. Finally, based on the sparse recovery results in the two domains of delay and slice, the jamming characteristics of ISRJ are identified and the jamming data is reconstructed to achieve the purpose of suppressing ISRJ. Furthermore, to address the potential impact of residual jamming on target recognition, we propose a robust method for the sparse representation of targets in the range domain. In contrast to traditional approaches, we have optimized the adaptive selection of regularization parameters, significantly improving the method's practicality. Combining this method with the PC results after jamming suppression can further enhance target recognition accuracy. Experimental results show that our method can effectively suppress ISRJ. Particularly, our method demonstrates stable anti-ISRJ performance when both the JDR and the total jammer SDR exceed 90%.

The structure of the paper is organized as follows. In Sect. 2, the signal model is introduced. In Sect. 3, an improved ISRJ parameter recovery and suppression method is proposed. In Sect. 4, numerical simulation experiments are presented to verify the effectiveness and analyze the performance. Finally, Sect. 5 presents some conclusions and discusses future work.

2 Signal model

2.1 Principle of ISRJ

The basic principle of ISRJ is shown in Fig. 1. When the DRFM operates in intermittent sampling storage mode, reconnaissance and jamming are performed alternately, with the jammer antenna operates asynchronously. The jammer first intercepts and samples the signal emitted by the radar. According to the research by Oliver [30], the current leading DRFM performance specifications are approximately an internal bandwidth of 800 MHz and 10 to 12 bits of ADC and DAC sampling at a frequency of 2000 MHz. This ensures high-fidelity sampling of radar emission signals by the DRFM. The jammer then retransmits the current sampled signal, continuing this process until the radar pulse
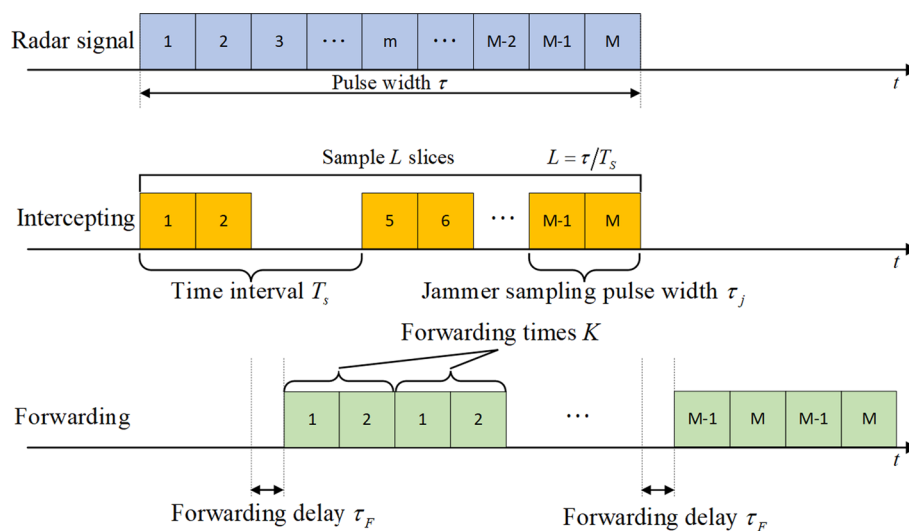

Fig. 1 Principle of ISRJ (Forwarding times $K = 2$)

transmission ceases. Assuming the jammer samples using a rectangular pulse sequence, the sampling timing can be specifically expressed as:

$$p(t) = \sum_{l=1}^{L} \text{rect}\left(\frac{t - (l-1)T_\text{s} - \frac{\tau_j}{2}}{\tau_j} \right) \tag{1}$$

where L represents the jammer sampling times. $T_\text{s} = \tau/L$ is the time interval of intercepted slices, and τ_j is the jammer sampling pulse width. Generally, τ_j remains fixed.

Assume that the radar transmits signal is $s(t)$, and there is a moving target with a radial velocity of v_s at the distance R_s from the radar. Then, the target signal echo can be expressed as:

$$x_s(t) = s\left(t - \tau_s + \frac{2v_s t}{c} \right) \tag{2}$$

where $\tau_s = 2R_s/c$ represents the real target delay and c is the speed of light. Correspondingly, the intercepted signal slices can be expressed as:

$$x_{sa}(t) = p(t - \tau_s)s\left(t - \tau_s + \frac{2v_s t}{c} \right) \tag{3}$$

The study in [31] reveals that by modulating the jamming slices with a fixed positive frequency, DRFM is able to change the position of the jamming peak after PC. This technique allows for the generation of advanced false target jamming, making it unreliable to distinguish between real and false targets based solely on time-delay. In light of this situation, the subsequent discussion in this paper is based on the assumption that the jammer modulates a fixed frequency-shift onto all jamming slices of the same forwarding within a single PRI. These modulated jamming slices are then continuously forwarded by the jammer K times, and thus, the forwarded signals from the jammer can be expressed as follows:

$$\begin{aligned} x_j(t) &= \sum_{k=1}^{K} x_{sa}\left(t - k\tau_j - \tau_F\right) \exp\left(j2\pi f_F t\right) \\ &= \sum_{k=1}^{K} p\left(t - \tau_s - k\tau_j - \tau_F\right)s\left(t - \frac{2(R_s - v_s t)}{c} - k\tau_j - \tau_F \right) \exp\left(j2\pi f_F t\right) \end{aligned} \tag{4}$$

where f_F represents the modulation frequency, and τ_F is the forwarding delay of the jammer.

By comparing (2) and (4), it can be seen that the modulation of radar signals mainly consists of three domains. Firstly, there is slice modulation: the intercepted signal slices contain only part of the sub-pulses of the original emitted signal, and our interest lies in identifying the specific positions of these sub-pulses in the original emitted signal. Secondly, time-delay modulation is involved: If the jammer does not apply additional modulation delay to the intercepted signal slices, then all the slices forwarded by the jammer on its kth forwarding within a single PRI can be considered as a composite signal, with the time-delay between these composite signals exactly equal to the jammer sampling pulse width τ_j. Lastly, there is frequency modulation:

Ji *et al. EURASIP Journal on Advances in Signal Processing*   (2024) 2024:55

Page 6 of 34

compared to the corresponding sub-pulses in the original emitted signal, the jamming sub-pulses exhibit a fixed modulation frequency-shift. Moreover, the Doppler caused by the radial movement of the target or jammer is also considered a form of frequency modulation. Therefore, by accurately estimating these three parameters, we can precisely reconstruct the jamming waveform. This discussion provides the possibility for effectively suppressing ISRJ from the perspectives of jamming reconstruction and cancellation.

2.2 Intra-pulse frequency agile waveform

Traditionally, the radar system emits linear-frequency modulation pulse with large time-bandwidth product to achieve high Doppler resolution and long-range detection. In order to design the dictionary matrix that satisfies the recoverable conditions, in this research, the LFM pulse is divided into M sub-pulses. By modulating the carrier frequency of these sub-pulses, the frequency bands between sub-pulses are staggered, and the sub-pulses are approximately orthogonal. Different from the traditional step frequency, the carrier frequency of the sub-pulse is not stepped sequentially, but arranged randomly. Therefore, the transmitted signal can be expressed as follows:

$$s(t) = \sum_{m=1}^{M} \text{rect}\left(\frac{t - (2m-1)\tau_{\text{sub}}/2}{\tau_{\text{sub}}}\right) \exp\left[j2\pi\left(f_0 + c_m\Delta f\right)t + j\pi\gamma t^2\right] \quad (5)$$

where τ_{sub} represents the sub-pulse width, f_0 refers to the carrier frequency. c_m is the frequency modulation code, Δf is the step size of the carrier frequency. The transmitted signal is shown in Fig. 2. The reasons for adopting intra-pulse frequency agile waveform will be discussed in detail in 3.4. In fact, we primarily take advantage of the ambiguity function characteristics of this type of waveform. As shown in Fig. 3, there is a significant difference between the ambiguity functions of stepped frequency LFM waveform and agile frequency LFM waveform. As mentioned in [22], the ambiguity function of
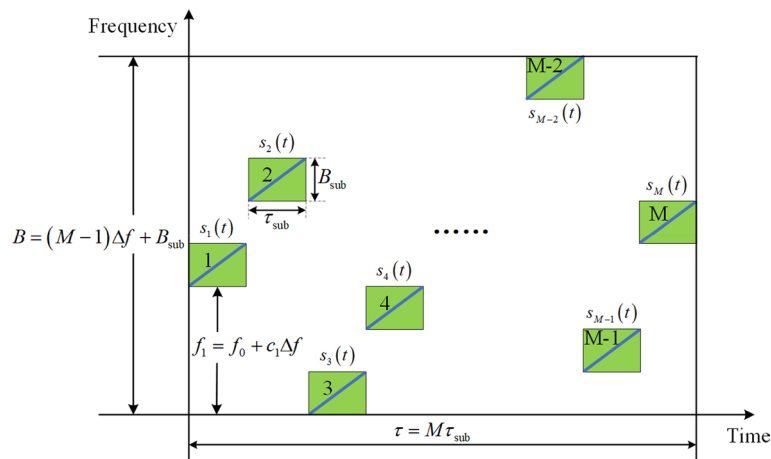

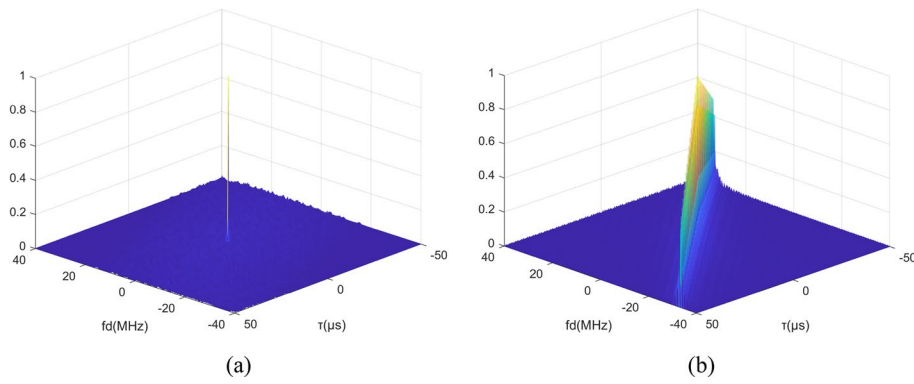**Fig. 2** Linear Frequency Modulation-Frequency Agile Waveform

Fig. 3 Ambiguity function: **a** Agile frequency LFM waveform. **b** Stepped frequency LFM waveform

the stepped frequency resembles a 'slanted knife-edge', indicating the presence of coupling between range and frequency-shift. In contrast, the ambiguity function of the agile frequency is closer to the ideal pushpin shape, showing lower sidelobe levels in both the zero-delay plane and the zero-frequency plane.

Therefore, the target echo after down-conversion received by the radar can be expressed as:

$$
\begin{aligned}
\hat{x}_s(t) &= s\left(t - \tau_s + \frac{2v_s t}{c}\right) \exp\left(-j2\pi f_0 t\right) \\
&= \sum_{m=1}^{M} A_m \mathrm{rect}\left(\frac{t - \tau_s - (2m-1)\tau_{\mathrm{sub}}/2}{\tau_{\mathrm{sub}}}\right) \exp\left[j2\pi f_d t + j2\pi c_m \Delta f t + j\pi\gamma(t-\tau_s)^2\right]
\end{aligned}
\tag{6}
$$

and the jamming echo after down-conversion can be expressed as:

$$
\begin{aligned}
\hat{x}_j(t) &= \sum_{k=1}^{K} x_{sa}\left(t - k\tau_j - \tau_F\right) \exp\left(j2\pi f_F t\right) \exp\left(-j2\pi f_0 t\right) \\
&= \sum_{k=1}^{K}\sum_{l=1}^{L}\sum_{m=1}^{M} A_{klm}\mathrm{rect}\left[\frac{t - (l-1)T_s - \tau_j/2 - \tau_s - k\tau_j - \tau_F}{\tau_j}\right] \\
&\quad \mathrm{rect}\left[\frac{t - (2m-1)\tau_{\mathrm{sub}}/2 - \tau_s - k\tau_j - \tau_F}{\tau_{\mathrm{sub}}}\right] \\
&\quad \cdot \exp\left[j2\pi f_d t + j2\pi c_m \Delta f t + j2\pi f_F t + j\pi\gamma\left(t - \tau_s - k\tau_j - \tau_F\right)^2\right]
\end{aligned}
\tag{7}
$$

When the sampling slice of the jammer happens to contain several complete subpulses, Eq. (7) can be simplified to:

$$
\begin{aligned}
\hat{x}_j(t) &= \sum_{k=1}^{K} x_{sa}\left(t - k\tau_j - \tau_F\right) \exp\left(j2\pi f_F t\right) \exp\left(-j2\pi f_0 t\right) \\
&= \sum_{k=1}^{K}\sum_{l=1}^{L}\sum_{m=1}^{M} A_{klm}\mathrm{rect}\left[\frac{t - (l-1)T_s - \tau_j/2 - \tau_s - k\tau_j - \tau_F}{\tau_j}\right] \\
&\quad \cdot \exp\left[j2\pi f_d t + j2\pi c_m \Delta f t + j2\pi f_F t + j\pi\gamma\left(t - \tau_s - k\tau_j - \tau_F\right)^2\right]
\end{aligned}
\tag{8}
$$

Therefore, the complete received echo $x(t)$ can be expressed as:

$$x(t) = \hat{x}_s(t) + \hat{x}_j(t) + n(t) \tag{9}$$

where $n(t)$ represents the white Gaussian noise.

3　Proposed method

3.1　Sparse recovery of ISRJ time-delay and frequency-shift

According to the analysis in Sect. 2.1 and 2.2, under the premise that the sub-pulse width is much shorter than the DRFM sampling pulse width, both the target echo and ISRJ can be regarded as a collection of partial transmitted signal sub-pulses modulated by time-delay and frequency-shift. In other words, the specific forms of the target and jamming echo can be determined by three parameters: time-delay, frequency-shift and the sub-pulse sequence number. If the jammer frequency-shift can be accurately estimated, then it is possible to extract the other two key parameters of ISRJ using sparse recovery techniques on the delay-slice plane, thereby effectively achieving jamming identification.

Based on the previous assumptions, all slices belonging to the same forwarding from the jammer have the same amount of frequency modulation within a single PRI. Thus, the jamming echo can be regarded as multiple synthetic signals equivalent to the number of forwarding K. For the two most common jamming modes: intermittent sampling direct forwarding and intermittent sampling repeated forwarding, to ensure strong coherence between the jamming echo and the real target echo, the jammer usually forwards each intercepted signal slice no more than 3 times. This implies that the sampling duty ratio of the jammer,which is also the duty ratio of the synthesized signal is at least 25%. Therefore, when estimating the frequency-shift parameter, these synthetic signals can be considered as target echoes that have undergone frequency shift modulation at different time delays. Additionally, these echoes only present as a few scatter points on the delay-frequency plane, exhibiting significant sparsity. Consider all possible time-delays and frequency-shifts in the echo, we assume that all time-delays are concentrated in $[\tau_{\min}, \tau_{\max}]$. By sampling it at an interval of $\Delta\tau$, the number of atoms in the time-delay domain is $N = (\tau_{\max} - \tau_{\min})/\Delta\tau + 1$. Similarly, all frequency-shifts are concentrated in $[f_{\min}, f_{\max}]$. By sampling it at an interval of Δf, the number of atoms in the frequency-shift domain is $J = (f_{\max} - f_{\min})/\Delta f + 1$. Thus, for the received P snapshots from t_1 to t_P, the following block model can be used for sparse representation:

$$\mathbf{X} = \Psi\alpha + \mathbf{N} \tag{10}$$

where $\mathbf{X} = [x(t_0), x(t_1), \cdots, x(t_P)]^{\mathrm{T}}$ is the received data, $\mathbf{N} = [n(t_1), n(t_2), \cdots, n(t_P)]^{\mathrm{T}}$ is the noise data. $\boldsymbol{\alpha} \in \mathbb{R}^{NJ}$ represents the unknown coefficient vector, which can be expressed as follows:

$$\boldsymbol{\alpha} = \left[\underbrace{\alpha_1[1], \cdots, \alpha_1[J]}_{\alpha_1}, \underbrace{\alpha_2[1], \cdots, \alpha_2[J]}_{\alpha_2}, \cdots, \underbrace{\alpha_N[1], \cdots, \alpha_N[J]}_{\alpha_N} \right]^{\mathrm{T}} \tag{11}$$

where α_n represents the nth block of $\boldsymbol{\alpha}$.

Furthermore, the block dictionary matrix $\boldsymbol{\Psi} \in \mathbb{C}^{P \times NJ}$ can also be expressed as a concatenation of column blocks $\boldsymbol{\Psi}_n \in \mathbb{C}^{P \times J}$:

$$
\boldsymbol{\Psi} = \left[\underbrace{\Psi_1[1], \cdots, \Psi_1[J]}_{\boldsymbol{\Psi}_1}, \underbrace{\Psi_2[1], \cdots, \Psi_2[J]}_{\boldsymbol{\Psi}_2}, \cdots, \underbrace{\Psi_N[1], \cdots, \Psi_N[J]}_{\boldsymbol{\Psi}_N} \right]^{\mathrm{T}} \tag{12}
$$

where $\Psi_n[q]$ is the qth column of $\boldsymbol{\Psi}_n$. $\Psi_n[q]$ is designed as the waveform atom corresponding to time-delay $\tau_n = \tau_{\min} + (n-1)\Delta\tau$ and frequency-shift $f_q = f_{\min} + (q-1)\Delta f$. Referring the transmitted signal shown in (5), it is designed as follows:

$$
\Psi_n[q] = \sum_{m=1}^{M} \mathrm{rect}\left[\frac{t - (2m-1)\tau_{\mathrm{sub}}/2 - \tau_n}{\tau_{\mathrm{sub}}} \right] \cdot \exp\left\{ j2\pi c_m \Delta f t + j2\pi f_q t + j\pi\gamma [t - \tau_n]^2 \right\} \tag{13}
$$

Although the window function in (13) may appear dissimilar to the function in (8), in reality, the former can be represented as a superposition of several instances of the latter. Therefore, employing the dictionary in Eq. (12) enables an accurate sparse representation of the jamming echo.

The structure of $\boldsymbol{\Psi}$ is shown in Fig. 4.

From (10), the coefficient vector $\boldsymbol{\alpha}$ can be recovered by solving the following problem:
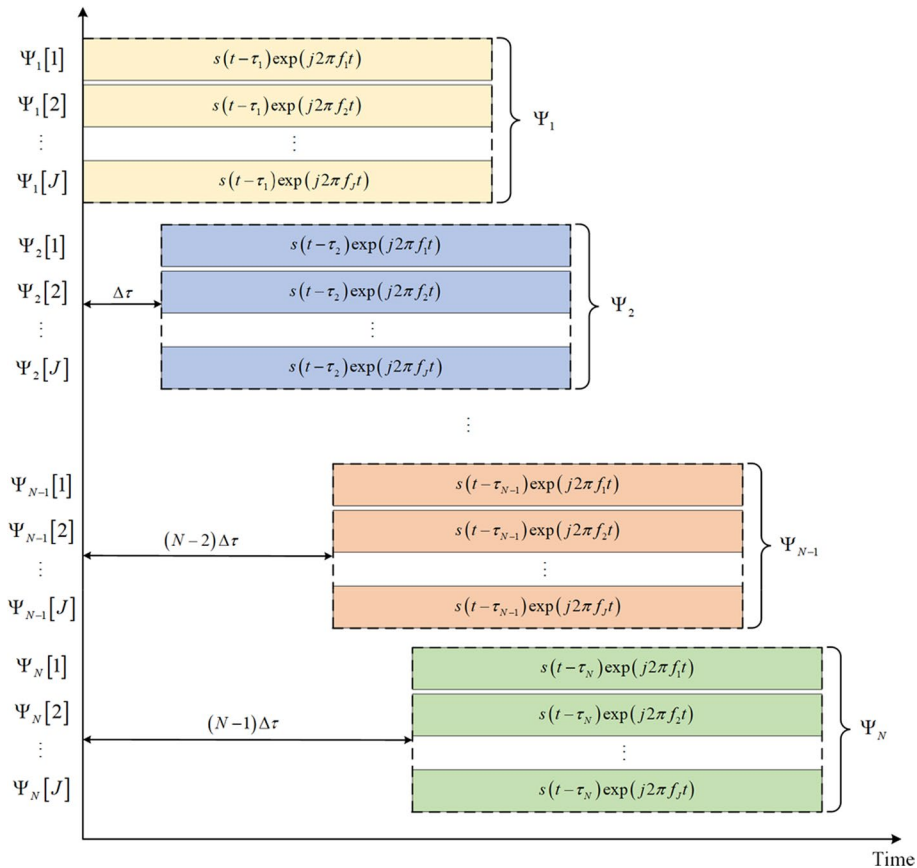

Fig. 4 The structure of delay-frequency dictionary

$$\min \|\boldsymbol{\alpha}\|_{2,0} \text{ s.t.} \|\mathbf{X} - \Psi\alpha\|_2 \leq \varepsilon \tag{14}$$

where $\|\boldsymbol{\alpha}\|_{2,0} = \sum_{n=1}^{N} I(\|\boldsymbol{\alpha}_n\|_2 > 0)$, $I(\cdot)$ represents the indicator function. To solve the NP hard problem like (14), it is usually approximated as the following problem in practice:

$$\min \|\boldsymbol{\alpha}\|_{2,1} \text{ s.t.} \|\mathbf{X} - \Phi\alpha\|_2 \leq \varepsilon \tag{15}$$

where $\|\boldsymbol{\alpha}\|_{2,1} = \sum_{n=1}^{N} \|\boldsymbol{\alpha}_n\|_2$. In 2010, Eldar proposed the block orthogonal matching pursuit (BOMP) algorithm [32], which is a fast solution to the above block sparsity problem. Typically, after the sparse reconstruction is completed, we can observe the target signal in the delay-frequency plane. The frequency shift of the target signal is usually zero, or equal to the Doppler frequency. Moreover, the jamming signal is composed of K synthesized signals of the same frequency modulation amount, and they appear as a few scattering points with the same frequency shift. The delay interval of these scattering points is equal to the sampling pulse width of the jammer. Therefore, by using the BOMP algorithm, the peak value generated by the jamming signal can be accurately located. The time-delay set $\tau_{Jam} \in \mathbb{C}^{K \times 1}$ and the frequency-shift amount f_{Jam} of the jammer synthetic signals can be effectively extracted.

3.2 Sparse recovery of ISRJ time-delay and sub-pulse

In the delay-frequency recovery process described in 3.1, we have determined the frequency shift modulation amount of the jammer. Despite this, the specific sequence numbers of each sub-pulse in the jamming echo are still unknown, which makes the specific forwarding mode of the jamming unclear. Therefore, in this section a more in-depth delay-slice sparse recovery of the jamming signal will be performed using the known information about the amount of jammer frequency modulation. The implementation of this recovery process is based on the following two core condition:

(i) Since all sub-pulses from the same forwarding share the same time-delay, the sub-pulses in the received echo occupy only a limited number of time-delay blocks. This number is determined by the number of forwarding from the jammer plus the number of targets. Based on this, we can achieve a sparse representation of the jamming signal on the delay-sub-pulse plane.

(ii) In practical scenarios, the intensity of the target echo is often lower than the noise intensity, which makes it more difficult to identify the delay block containing the target echo. However, the intensity of the interfering signal fragments usually exceeds that of the target signal, which means that the interfering sub-pulses are easier to detect and locate on the delay-sub-pulse plane, thus making the parameter estimation of the interfering sub-pulses more accurate.

Therefore, the delay-slice block sparse model can be constructed as:

$$\mathbf{X} = \Phi\beta + \mathbf{N} \tag{16}$$

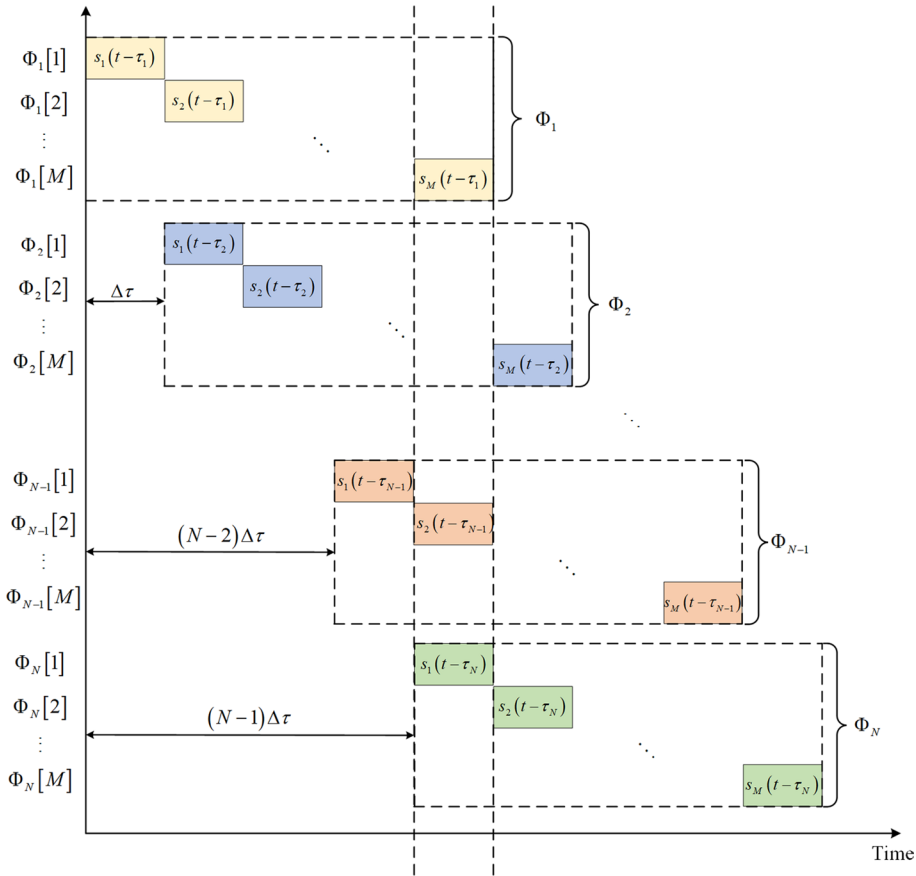where $\boldsymbol{\beta} \in \mathbb{R}^{NM}$ represents the coefficient vector, which can be expressed as:

Fig. 5 The structure of delay-slice dictionary

$$\boldsymbol{\beta} = \left[\underbrace{\beta_1[1], \cdots, \beta_1[M]}_{\boldsymbol{\beta}_1}, \underbrace{\beta_2[1], \cdots, \beta_2[M]}_{\boldsymbol{\beta}_2}, \cdots, \underbrace{\beta_N[1], \cdots, \beta_N[M]}_{\boldsymbol{\beta}_N}\right]^{\mathrm{T}} \quad (17)$$

where $\boldsymbol{\beta}_n$ represents the nth block of $\boldsymbol{\beta}$.

Similarly, the block dictionary matrix $\boldsymbol{\Phi} \in \mathbb{C}^{P \times NM}$ can also be expressed as the concatenation of column blocks $\boldsymbol{\Phi}_n \in \mathbb{C}^{P \times M}$:

$$\boldsymbol{\Phi} = \left[\underbrace{\Phi_1[1], \cdots, \Phi_1[M]}_{\boldsymbol{\Phi}_1}, \underbrace{\Phi_2[1], \cdots, \Phi_2[M]}_{\boldsymbol{\Phi}_2}, \cdots, \underbrace{\Phi_N[1], \cdots, \Phi_N[M]}_{\boldsymbol{\Phi}_N}\right]^{\mathrm{T}} \quad (18)$$

where $\Phi_n[m]$ is the mth column of $\boldsymbol{\Phi}_n$. The structure of $\boldsymbol{\Phi}$ is shown in Fig. 5.

The setting of $\boldsymbol{\Phi}$ is similar to $\boldsymbol{\Psi}$, but the difference is that the atoms within the block are set to correspond to different sub-pulses under the block delay. Therefore, $\Phi_n[m]$ is designed as the waveform atom corresponding to time-delay $\tau_n = \tau_{\min} + (n-1)\Delta\tau$ and the mth sub-pulse. However, this design does not consider the influence of frequency-shift. Using the time-delay and frequency-shift information of the jamming synthetic

signal obtained in 3.1, the waveforms of the sub-pulses in the time-delay block where the jamming echo is located can be corrected in batches. Therefore, $\Phi_n[m]$ can be expressed as follows:

$$
\Phi_n[m] = \begin{cases} \mathrm{rect}\left\{ \frac{t-(2m-1)\tau_{\mathrm{sub}}/2-\tau_n}{\tau_{\mathrm{sub}}} \right\} \exp\left\{ j2\pi c_m \Delta f(t-\tau_n) + j2\pi f_{Jam}(t-\tau_n) + j\pi\gamma[t-\tau_n]^2 \right\} \, \tau_n \in \tau_{Jam} \\ \mathrm{rect}\left\{ \frac{t-(2m-1)\tau_{\mathrm{sub}}/2-\tau_n}{\tau_{\mathrm{sub}}} \right\} \exp\left\{ j2\pi c_m \Delta f(t-\tau_n) + j\pi\gamma[t-\tau_n]^2 \right\} \, \tau_n \notin \tau_{Jam} \end{cases}
$$

$$(19)$$

Similar to (15), the solution of $\boldsymbol{\beta}$ can be transformed into the following problem:

$$
\min \|\boldsymbol{\beta}\|_{2,1} \text{ s.t.} \|\mathbf{X} - \Phi\beta\|_2 \leq \varepsilon \tag{20}
$$

After applying the BOMP method to solve the block sparse problem, the jamming slices can be identified on the recovered delay-slice plane according to the following characteristics:

(i) *Target echo* The target echo contains all sub-pulses in the transmitted signal. The time-delay of these sub-pulses is equal to the real target time-delay. Therefore, on the delay-slice plane, the target echo appears as a continuous envelope. This continuous envelope is formed due to the ability of the target echo to retain the time-intact structure of the transmitted signal.

(ii) *Jamming echo* On the contrary, because the jamming slices belonging to the same forwarding have the same time-delay modulation amount, the jamming echo appears as K discontinuous envelopes on the plane. The JDR of these discontinuous envelopes is equal to the sampling duty ratio of the jammer. In addition, the energy of jamming signal is usually significantly stronger than the background noise, making the jamming echo more conspicuous on the plane.

(iii) *Noise* In contrast, noise appears on the delay-slice plane as a scattered envelope distributed over the entire block, with an irregular amplitude distribution, thereby contrasting with target echo and jamming echo.

In summary, if the duty ratio of a block is between 20 and 60%, and its energy is significantly higher than the noise level, then the recovered sub-pulses on the block can be considered to correspond to ISRJ.

3.3 Jamming cancelation and target extraction

Based on the estimated time-delay and sub-pulse sequence number of ISRJ, all sub-pulses in each jamming block can be reconstructed and integrated into $\boldsymbol{\Theta}$, by which ISRJ can be linearly represented. The jamming amplitude vector $\boldsymbol{\gamma}$ can be calculated by LS (linear solution):

$$
\boldsymbol{\gamma} = \left(\boldsymbol{\Theta}^{\mathrm{H}}\boldsymbol{\Theta} \right)^{-1} \boldsymbol{\Theta} x \tag{21}
$$

Although there is a slight error in the estimation of jamming amplitude, this does not prevent the effective suppression of most jamming slices. After the jamming cancellation is completed, only sporadic jamming fragments remain in the received echo, further enhancing the waveform difference between the jamming echo and the radar transmitted waveform. Such changes mean that the jamming echo cannot approximate

the original transmit waveform through simple time-delay modulation. In addition, the energy of these residual jamming slices is weakened but still higher than the target echo, and can be treated as a stronger noise signal during processing.

Thus, the remaining signal $\hat{\mathbf{x}}$ can be expressed as:

$$
\begin{aligned}
\hat{\mathbf{X}} &= \hat{\mathbf{X}} - \Theta\gamma \\
&= \hat{\mathbf{X}}_s + \left(\hat{\mathbf{X}}_j - \Theta\gamma\right) + \mathbf{N} \\
&= \hat{\mathbf{X}}_s + \hat{\mathbf{N}}
\end{aligned}
\tag{22}
$$

It can be seen that the real target is still submerged in strong noise after jamming suppression. Although this kind of noise exhibits the characteristics of color noise, its waveform is still significantly different from the echo waveform of the real target. In addition, real targets show sporadic and discontinuous distribution characteristics in the time-delay domain. Therefore, we propose to transform the real target detection problem into a sparse recovery problem by sparsely representing the processed echo signal in the time-delay domain. The corresponding sparse model can be expressed as:

$$
\hat{\mathbf{X}} = \hat{\Phi}\xi + \hat{\mathbf{N}}
\tag{23}
$$

where ξ is the coefficient vector. $\hat{\Phi} \in \mathbb{C}^{P \times N}$ represents the time-delay dictionary matrix, which can be expressed as:

$$
\hat{\Phi}_n = \sum_{m=1}^{M} \mathrm{rect}\left(\frac{t - (2m-1)\tau_{\mathrm{sub}}/2 - \tau_n}{\tau_{\mathrm{sub}}}\right) \exp\left[j2\pi c_m \Delta f(t - \tau_n) + j\pi\gamma(t - \tau_n)^2\right]
\tag{24}
$$

which is actually the sum of atoms in Φ_n. The design of $\hat{\Phi}$ does not consider the influence of the Doppler effect, because the phase change caused by the Doppler frequency within a single PRI is small, and the impact on the waveform envelope is negligible.

In 2016, Chen et al. proposed the adaptive regularized smoothing l0 norm algorithm (AReSl0) [33, 34]. This method is specifically designed to handle robust sparse recovery problems such as (23). The core idea is to use the Gaussian function family to approximate the discontinuous l0 norm, thus transform solving (23) into an optimization problem with constraints. According to the philosophy of this method, the coefficient vector ξ can be reconstructed by solving the following problem:

$$
\begin{cases}
\min\limits_{\xi} F_\sigma(\xi) \\
\mathrm{s.t.} \left\|\hat{\mathbf{X}} - \hat{\Phi}\xi\right\|_2^2 < \varepsilon
\end{cases}
\tag{25}
$$

where $F_\sigma(\xi) = \sum\limits_{i=1}^{N} f_\sigma(\xi_i)$. In fact, f_σ can be any family of functions that approaches the Kronecker-Delta function, such as the family of Gaussian functions. ε represents the noise level.

A small σ results in multiple local maxima for $F_\sigma(\xi)$, which makes it difficult to apply the steepest descent method to find the global optimal solution. Fortunately, $F_\sigma(\xi)$ will smooth out as σ increases. Therefore, we design a nested loop, and adapt a large value of σ at the beginning of the external loop to avoid the iterative solution from falling into

Ji *et al. EURASIP Journal on Advances in Signal Processing*   (2024) 2024:55

Page 14 of 34

a local optimum. As σ decreases, $F_\sigma(\xi)$ will more accurately approximate the l_0 norm. The internal loop iterates a small fixed value, which can be described as the following two steps: Firstly, iteratively optimizes the solution of the coefficient matrix through the steepest descent algorithm, then projects the solution into the feasible set. In the first step, the iterative form of the steepest descent method is:

$$\tilde{\tilde{\xi}} \leftarrow \xi + \mu_j \nabla F_\sigma(\xi) \tag{26}$$

where $\tilde{\tilde{\xi}}$ represents the iterative solution and $\nabla F_\sigma(\xi)$ is the derivative of $F_\sigma(\xi)$. The step μ_j should be proportional to σ^2, we choose a fixed constant μ such that $\mu_j = \mu\sigma^2$.

The iterative solution $\hat{\xi}$ obtained by the first step does not satisfy the constraints of (25), so it needs to be projected into the feasible set, which is equivalent to solve the following optimization problem:

$$\begin{cases} \min_{\xi} \left\| \xi - \hat{\xi} \right\|_2 \\ \text{s.t.} \left\| \hat{\Phi}\xi - \hat{\mathbf{X}} \right\|_2^2 < \varepsilon \end{cases} \tag{27}$$

A common solution to (27) is the Lagrange multiplier method, and the Lagrange form of (27) is:

$$J(\xi) = \left\| \xi - \hat{\xi} \right\|_2^2 + \lambda \left\| \hat{\Phi}\xi - \hat{\mathbf{X}} \right\|_2^2 \tag{28}$$

where λ represents the regularization parameter, it is used to balance the sparsity and residual fitting ξ. Then the projection solution $\xi^{(j)}$ can be calculated by the weighted least squares (WLS):

$$\xi = \hat{\xi} - \hat{\Phi}^{\mathrm{H}} \left(\hat{\Phi}\hat{\Phi}^{\mathrm{H}} + \lambda^{-1}\boldsymbol{I}_P \right)^{-1} \left(\hat{\Phi}\hat{\xi} - \hat{\mathbf{X}} \right) \tag{29}$$

The update of regularization parameter λ directly affects the recovery performance. However, Chen et al. did not provide a suitable method for selecting the regularization parameter in [34]. Therefore, we design an adaptive iterative method for the update of λ. Since the number of iterations in the internal loop is small and fixed, λ is updated along with the external loop. It can be seen from (28) that the former term of $J(\xi)$ is used to control the approximation of the solution to the steepest descent solution, aiming to ensure the sparsity of the result. The latter term is the regularization term that minimizes the residual. Therefore, an ideal λ should balance the sparsity and robustness of the solution, The partial derivative of $J(\xi)$ can be calculated by the following formula:

$$\frac{\partial J(\xi)}{\partial \xi} = 2\left(\xi - \hat{\xi} \right) + 2\lambda \left(\hat{\Phi}^{\mathrm{H}}\hat{\Phi}\xi - \hat{\Phi}^{\mathrm{H}}\hat{\mathbf{X}} \right) \tag{30}$$

Let $\frac{\partial J(\xi)}{\partial \xi} = 0$ then taking the l_2 norm of the both sides of the equation, we have:

$$\lambda = \frac{\left\| \xi - \hat{\xi} \right\|_2}{\left\| \hat{\Phi}^H \hat{\Phi} \xi - \hat{\Phi}^H \hat{X} \right\|_2} \tag{31}$$

The projected solution ξ in (31) is an unknown prior. The projected solution $\xi^{(j-1)}$ of the $j - 1^{th}$ external loop is chosen as its replacement in [34], then λ can be estimated by:

$$\hat{\lambda}_j = \frac{\left\| \xi^{(j-1)} - \hat{\xi}^{(j)} \right\|_2}{\left\| \hat{\Phi}^H \hat{\Phi} \xi^{(j-1)} - \hat{\Phi}^H \hat{X} \right\|_2} \tag{32}$$

where $\hat{\xi}^{(j)}$ represents the iterative solution of the jth loop. However, it will bring the following two problems:

(i)   In general, large λ corresponds to small σ [34]. σ is a large value under strong noise. For the initial solution ξ_0, the minimum norm solution with $\hat{X} = \hat{\Phi}\xi$ is generally selected as the initial solution, which causes the denominator of (32) to be a very small value, resulting in the initial solution $\hat{\lambda}_1$ being too large.

(ii) Since the projection solution $\xi^{(j-1)}$ of $j - 1^{th}$ external loop satisfies the following equation:

$$\left(\xi^{(j-1)} - \hat{\xi}^{(j-1)} \right) + \hat{\lambda}_{j-1} \left(\hat{\Phi}^H \hat{\Phi} \xi^{(j-1)} - \hat{\Phi}^H \hat{X} \right) = 0 \tag{33}$$

Equation (32) can be simplified to $\hat{\lambda}_j = u_{j-1} \hat{\lambda}_{j-1}$, where u_{j-1} is the iteration factor. It can be expressed as:

$$u_{j-1} = \frac{\left\| \left(\hat{\xi}^{(j)} - \xi^{(j-1)} \right) \right\|_2}{\left\| \left(\xi^{(j-1)} - \hat{\xi}^{(j-1)} \right) \right\|_2} \tag{34}$$

where $\left(\hat{\xi}^{(j)} - \xi^{(j-1)} \right)$ represents the variation of the gradient solution in the jth external loop, $\left(\xi^{(j-1)} - \hat{\xi}^{(j-1)} \right)$ represents the variation of the projection solution in the $j - 1^{th}$ external loop. It can be seen that $\hat{\lambda}$ is not strictly decreasing.

The above two points make it difficult for $\hat{\lambda}$ to converge to an appropriate order of magnitude. Therefore, we give the following iterative formula:

$$\hat{\lambda}_j = \frac{\left\| \xi^{(j-1)} - \hat{\xi}^{(j)} \right\|_2}{\left\| \hat{\Phi}^H \hat{\Phi} \hat{\xi}^{(j)} - \hat{\Phi}^H \hat{X} \right\|_2} \tag{35}$$

by replacing $\xi^{(j-1)}$ in the denominator with $\hat{\xi}^{(j)}$, the problem of too large initial solution is solved. Compared with $\xi^{(j-1)}$, the new expression contains the gradient information of this loop, which is closer to the estimated value of $\xi^{(j)}$. Therefore, the new $\hat{\lambda}_j$ is more accurate than the traditional method. The pseudocode of the optimized robust SL0 algorithm is shown in Algorithm 1.

Algorithm 1 The optimized robust SL0 algorithm

Input: Received data $\hat{\mathbf{X}}$; Dictionary $\hat{\boldsymbol{\Phi}}$.

Output: Recovered coefficient vector ξ .

Initialization

    Let $\xi_0 = \hat{\boldsymbol{\Phi}}^{\mathrm{H}} \left(\hat{\boldsymbol{\Phi}} \hat{\boldsymbol{\Phi}}^{\mathrm{H}} \right)^{-1} \hat{\mathbf{X}}$.

    Select an appropriate descending sequence for σ, $\left[\sigma_1, \sigma_2, \ldots, \sigma_J \right]$.

    for $j = 1, 2, \ldots, J$

        Let $\sigma = \sigma_j$.

        Let $\xi = \xi_{j-1}$

        for $g = 1, 2, \ldots, G$

            Maximize $F_\sigma \left(\xi \right)$ using the steepest ascent algorithm:

            Calculate $\hat{\xi} = \xi + \mu \sigma^2 \nabla F_\sigma \left(\xi \right)$

            Update regularization parameter $\hat{\lambda}$:

            if $g = 1$ **then**

                Calculate $\hat{\lambda}$ by (35)

            end if

            Project $\hat{\xi}$ back onto the feasible set $\left\| \hat{\boldsymbol{\Phi}} \xi - \hat{\mathbf{X}} \right\|_2^2 < \varepsilon$:

            $\xi = \hat{\xi} - \hat{\boldsymbol{\Phi}}^{\mathrm{H}} \left(\hat{\boldsymbol{\Phi}} \hat{\boldsymbol{\Phi}}^{\mathrm{H}} + \lambda^{-1} \mathbf{I}_P \right)^{-1} \left(\hat{\boldsymbol{\Phi}} \hat{\xi} - \hat{\mathbf{X}} \right)$

        end for

        Set $\xi^{(j)} = \xi$

    end for

    $\xi = \xi^{(J)}$

    return ξ

By using the optimized robust sparse recovery algorithm, the coefficient vector ξ can be stably restored even in a strong noise environment. Finally, referring to the recovery results and the PC results after jamming suppression, the real target is accurately detected and its position information is extracted. The flowchart of the proposed method is shown in Fig. 6.

3.4 Recovery condition

In this section, we discuss the recovery condition of block sparse model and regular sparse model respectively.

3.4.1 Recovery condition of block model

The restricted isometric property is a common criterion for evaluating the recovery capabilities of dictionary matrices. In 2010, Eldar proposed that for the block models such as (10), to be stably restored by BOMP, the sufficient condition is [32]:

$$UJ < \frac{1}{2} \left(\mu_B^{-1} + J - (J+1)\mu_S \mu_B^{-1} \right) \tag{36}$$

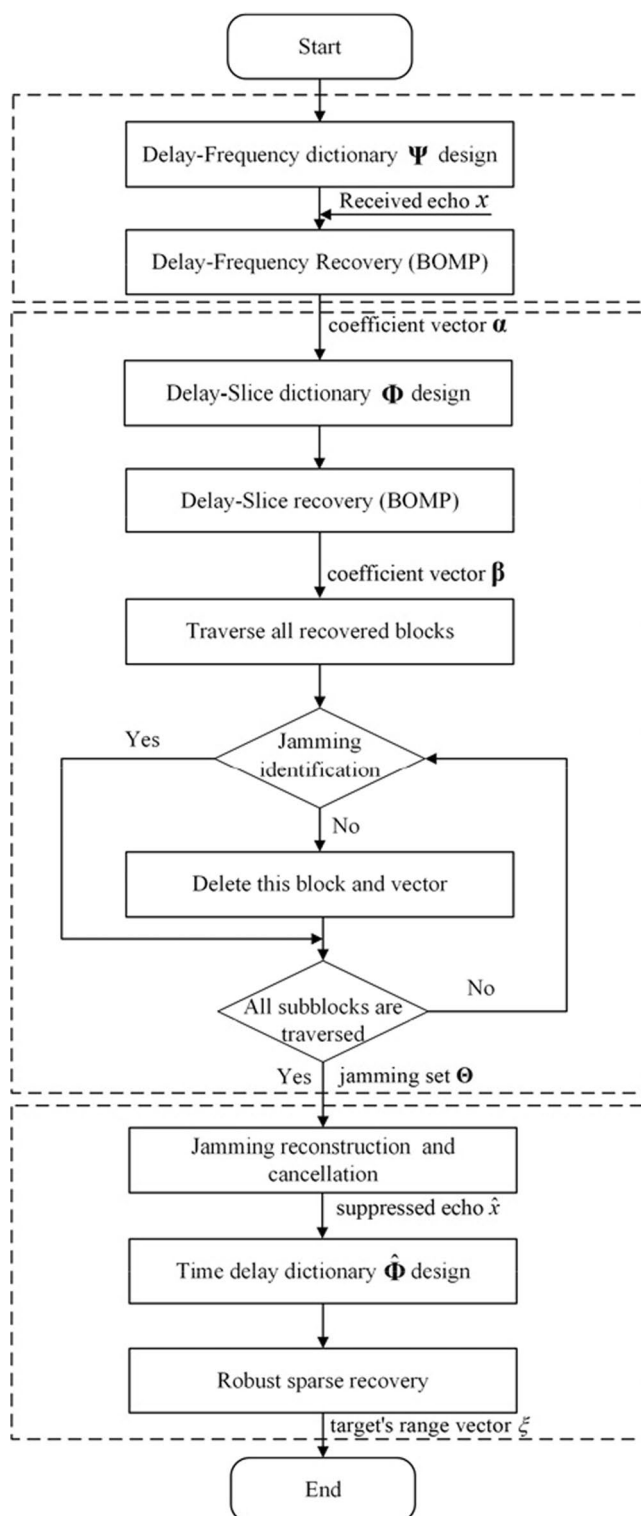where U is the block sparsity. μ_S represents the sub-coherence, which is defined as:

Fig. 6 Flowchart of the proposed method

$$\mu_S = \max_l \max_{i,j \neq i} \left| \Psi_l[i]^{\mathrm{H}} \Psi_l[j] \right| \tag{37}$$

μ_S is used to measure the similarity between sub-pulses. In order to satisfy the recovery condition, μ_S should be as low as possible. $\Psi_l[i]$ represents the echo signal with time-delay τ_l and frequency modulation f_i. Therefore, $\Psi_l[i]^{\mathrm{H}} \Psi_l[j]$ represents the correlation between echoes with the frequency modulation f_i and f_j under the same time-delay, which is essentially equivalent to the transmitted signal's ambiguity function with zero time-delay and the Doppler of $f_i - f_j$. Therefore, in order to design intra-block atoms with low sub-coherence, it is critical to ensure that the side lobes of the Doppler plane of the transmitted waveform ambiguity function at zero delay are low.

μ_B represents the block-coherence, it is defined as:

$$\mu_B = \max_{l,r \neq l} \frac{1}{J} \lambda_{\max}^{1/2} \left[\left(\boldsymbol{\Phi}_l^{\mathrm{H}} \boldsymbol{\Phi}_r \right)^{\mathrm{H}} \left(\boldsymbol{\Phi}_l^{\mathrm{H}} \boldsymbol{\Phi}_r \right) \right] \tag{38}$$

μ_B is used to measure the similarity between time-delay blocks. In order to satisfy the recoverability condition, μ_B should be as low as possible. From an intuitive point of view, the block-coherence of the dictionary matrix $\boldsymbol{\Psi}$ reflects the correlation between echoes with different time-delays and frequency modulations. Similar to the analysis of μ_S, if the transmitted waveform exhibits low side-lobe characteristics on both time-delay plane and Doppler plane, low block-coherence can be ensured.

Similar to (10), the recovery condition of (16) can also be defined by the sufficient condition in (36). $\boldsymbol{\Phi}_l[i]$ represents the ith sub-pulse echo with time-delay τ_l. Considering that the frequency bands between sub-pulses are staggered from each other, it can be reasonably assumed that these sub-pulses are approximately orthogonal, so their sub-coherence is close to zero. In addition, the block-coherence of dictionary matrix $\boldsymbol{\Phi}$ reflects the correlation between transmitted waveforms at different time-delays. Different from the stepped frequency waveform, the sub-pulse frequency bands of the agile frequency waveform are randomly distributed. This feature significantly reduces the similarity of waveforms under different time-delays, thereby ensuring low block-coherence of $\boldsymbol{\Phi}$.

3.4.2 Recovery condition of regular model

Calculating the RIP constant of a given dictionary matrix is very challenging, but in recent years a friendlier property has emerged—Mutual Incoherence Property (MIP). It has been widely applied in analyzing the performance guarantees of sparse recovery algorithms. Simply put, if a matrix satisfies the MIP condition, then the performance of the sparse recovery algorithms is theoretically guaranteed. Typically, discussing the MIP property of a matrix is easier than its RIP property. The maximum coherence coefficient of the dictionary matrix $\hat{\boldsymbol{\Phi}}$ is defined as:

$$\mu\left(\hat{\boldsymbol{\Phi}} \right) = \max_{0 \leq i \neq j \leq N-1} \frac{\left| \left\langle \hat{\boldsymbol{\Phi}}_i, \hat{\boldsymbol{\Phi}}_j \right\rangle \right|}{\left\| \hat{\boldsymbol{\Phi}}_i \right\|_2 \left\| \hat{\boldsymbol{\Phi}}_j \right\|_2} \tag{39}$$

If $\mu\left(\hat{\Phi}\right) < \frac{1}{2U-1}$, then $\hat{\Phi}$ has the MIP property and can be recovered stably. Since $\hat{\Phi}_i$ represents the signal echo of time-delay τ_i, $\mu\left(\hat{\Phi}\right)$ is equivalent to the highest side lobe of the transmitted waveform ambiguity function on the time-delay plane. Therefore, if the ambiguity function of the transmitted waveform has a low time-delay plane side lobe, then $\hat{\Phi}$ can be stably recovered.

Based on the above analysis, in order to ensure the stability of the three sparse recovery processes proposed in this article, it is necessary to ensure that the transmitted waveform meets a series of specific conditions. These conditions mainly involve the ambiguity function of the transmitted waveform, requiring its side-lobe levels to be kept low in the time-delay plane and Doppler plane. In addition, the frequency bands of each sub-pulse in the transmitted waveform should be appropriately staggered. The ambiguity function of the agile frequency LFM waveform shown in Fig. 3 presents a unique "pushpin" shape. This feature ensures that the recovery conditions are met and provides an important guarantee for achieving stable sparse recovery.

4 Experiments

4.1 Analysis of block sparse recovery results

In this section, we first explore the characteristic differences between the target and ISRJ on the delay-frequency plane and the delay-slice plane under noise-free conditions. Please refer to Table 1 for specific parameter settings. During the two rounds of sparse recovery, we set the following meshing parameters: $\tau_{\min}$ and $\tau_{\max}$ are chosen as $1000\mu s$ and $1100\mu s$, with an interval of $1\mu s$, so there were a total of grids in the time-delay domain. $f_{\min}$ and $f_{\max}$ are chosen as 0 MHz and 20 MHz, with an interval of 0.2 MHz, so there were a total of grids in the frequency-shift domain. This is mainly because in order to ensure that the false target after PC is ahead of the real target, the frequency modulation amount of the jammer is positive and maintained at the MHz level. In order to ensure that the jammer can sample sub-pulses approximately completely, we set the number of sub-pulses to M = 100, and the pulse width of each sub-pulse is 1us. The two sparse recovery processes share the same sparsity upper limit U, and the specific value of this parameter will be determined according to the actual application scenario. All simulation experiments are conducted on a personal computer equipped with a 3.2 GHz i7 CPU and 32 GB RAM (Table 1).

As shown in Fig. 7, the delay-frequency recovery results of the target and ISRJ with two different forwarding times are shown. In the delay-frequency plane analysis, the target appears as a single peak, and since it is not frequency modulated, its frequency-shift amount is zero. In contrast, the peak number of ISRJ depends on the forwarding time of the jammer. Specifically, jamming 1 only produces a peak value of nonzero frequency-shift in the plane. Jamming 2 presents three peaks with similar amplitudes and the same amount of frequency-shift. It is worth noting that since all jamming slices for each forwarding are treated as a complete target in the modeling, this causes the recovered peak amplitude to decrease relatively as the forwarding time increases. However, in order to ensure the coherence of the jamming, the jammer limits the forwarding time, thus ensuring the effectiveness of the recovery process.

Table 1 Parameters settings of radar and source

Parameter	Value
Pulse duration	100 μs
Number of sub-pulses	100
Sub-pulse bandwidth	0.5 MHz
Agile bandwidth	0.5 MHz
Synthetic bandwidth	99.5 MHz
Sampling frequency	200 $textMHz$
Target	
Time-delay	1050 μs
Modulation frequency	0 MHz
Jammer 1	
Forwarding time	1
Modulation delay	2 μs
Modulation frequency	8 MHz
Jammer 2	
Forwarding time	3
Modulation delay	4 μs
Modulation frequency	16 MHz
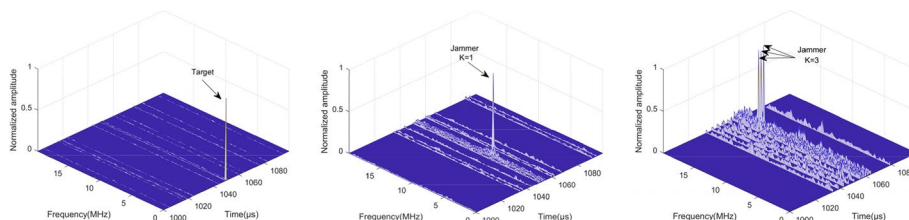
Fig. 7 Delay-frequency recovery result, from left to right: Real target, ISRJ ($K = 1$), ISRJ ($K = 3$)
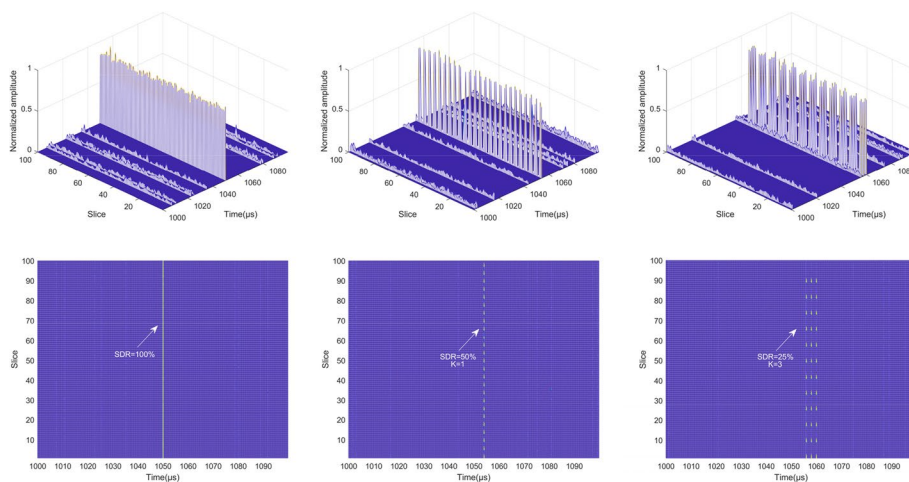
Fig. 8 Delay-slice recovery result, Top (from left to right): Real target, ISRJ ($K = 1$), ISRJ ($K = 3$) Bottom (from left to right): Top view of the Delay-slice plane

Ji *et al. EURASIP Journal on Advances in Signal Processing*   (2024) 2024:55

Page 21 of 34

Figure 8 shows the delay-slice recovery results. Observing the delay-slice plane, the recovered target sub-pulses are concentrated in the same block. The performance is continuous distribution and similar amplitude, indicating that the SDR is close to 100%. For ISRJ in direct forwarding mode, the recovered jamming sub-pulses are all concentrated in a single block, the sub-pulse sequence numbers are discontinuous, and the JDR is equal to the jammer SDR of 50%. Due to the asynchronous operating characteristics of DRFM, the time-delay of this block is equal to the sum of the target delay, jammer modulation delay and jammer sampling pulse width. For ISRJ in repeated forwarding mode, the recovered jamming pulses are distributed in $K = 3$ blocks. Since the jamming pulses on each block originate from the same set of signal slices intercepted by the jammer, the sub-pulse sequence numbers of each block are the same. Thus, the JDR on each block is equivalent to the jammer SDR of 33%. In addition, the last $K - 1$ jamming blocks can be regarded as equal delay translations of the first jamming block, and their intervals are the jammer sampling pulse width.

Discussing the iteration stop conditions of BOMP is crucial. Since all jamming slices from the same forwarding are treated as a composite signal during the block recovery process, the block sparsity of ISRJ remains consistent across both block models, a fact that is validated in Figs. 7 and 8. For instance, for direct-forward jamming, a sharp peak can be recovered on the delay-Doppler plane, and a series of envelopes can be recovered on the delay-slice plane. For repeated-forward jamming (forwarding times = 3), three sharp peaks can be recovered on the delay-Doppler plane, and three series of envelopes can be recovered on the delay-slice plane. Based on this, we set a reasonable sparsity upper limit U, which should be greater than the total number of forwarding times by all jammers in the scene. If the number of iterations reaches U, the iteration stops. Moreover, since the preset sparsity limit exceeds the actual sparsity, some blocks recovered incorrectly containing only noise are identified in the last few iterations. Therefore, if the residual energy is lower than the noise energy E_n in the ith iteration, or if the number of iterations reaches the sparsity limit U, the iteration will stop.

4.2 Examples in three scenarios

In this section, we constructed three scenarios containing different jamming distributions and conducted a comparative analysis between our method and the Costas-SPC method proposed in [23] to verify the effectiveness and superiority of our method. It

Table 2 Parameters settings of scenario 1

Parameter	Value
Target	
Time-delay	1050 µs
SNR	−10 dB
Jammer 1	
Forwarding time	1
Modulation delay	2 µs
Modulation frequency	8 MHz
JNR	20 dB

is worth pointing out that the basic idea of Costas-SPC method is to decompose the broadband filter into a set of narrowband filters, remove the filter output of the signal fragment sampled by the jammer, and accumulate and process the output of the remaining filters. This method has certain similarities with the method of this study in terms of waveform design. First, we considered a simple scenario containing a single target and a single jammer, with parameter settings as shown in Table 2. In this case, the SDR of a single jammer on the transmitted signal is 50%, and the JDR in the echo data is also 50%. As shown in Fig. 9a, on the delay-frequency plane, the jamming appears as a single peak with specific frequency modulation. However, the peak value of the target is very weak, so it is difficult to estimate the parameters of the target directly on this plane. Figure 9b, c and d shows the recovered delay-slice plane and the corresponding jamming identification results, respectively. It can be seen that the ISRJ appears as a series of discontinuous envelopes with the same modulation time-delay on this plane. These envelopes have a 50% duty ratio on the block with 1054μ*s* and similar amplitudes. Figure 9e and f shows the jamming distribution before and after cancellation, respectively. The results show that the energy of the jamming before cancellation is much greater than the target signal, but 50% of the target signal is not covered by the ISRJ. After cancellation, the jamming intensity is effectively reduced to the same magnitude as the target echo. Therefore, the real target can be detected after PC at a time-delay of 1050μ*s*.
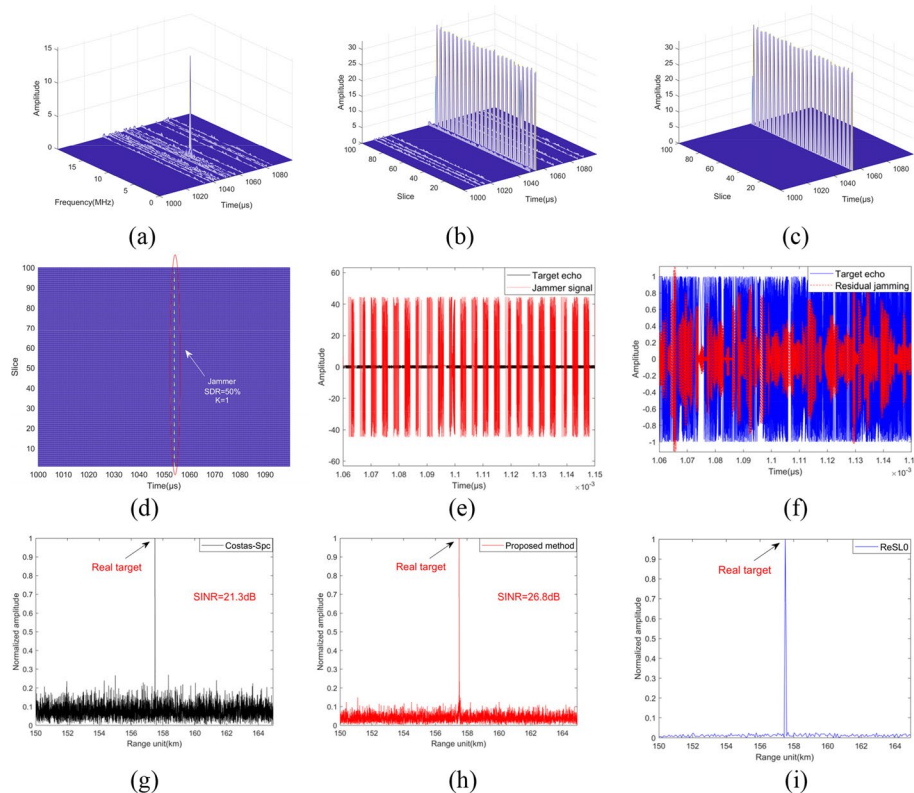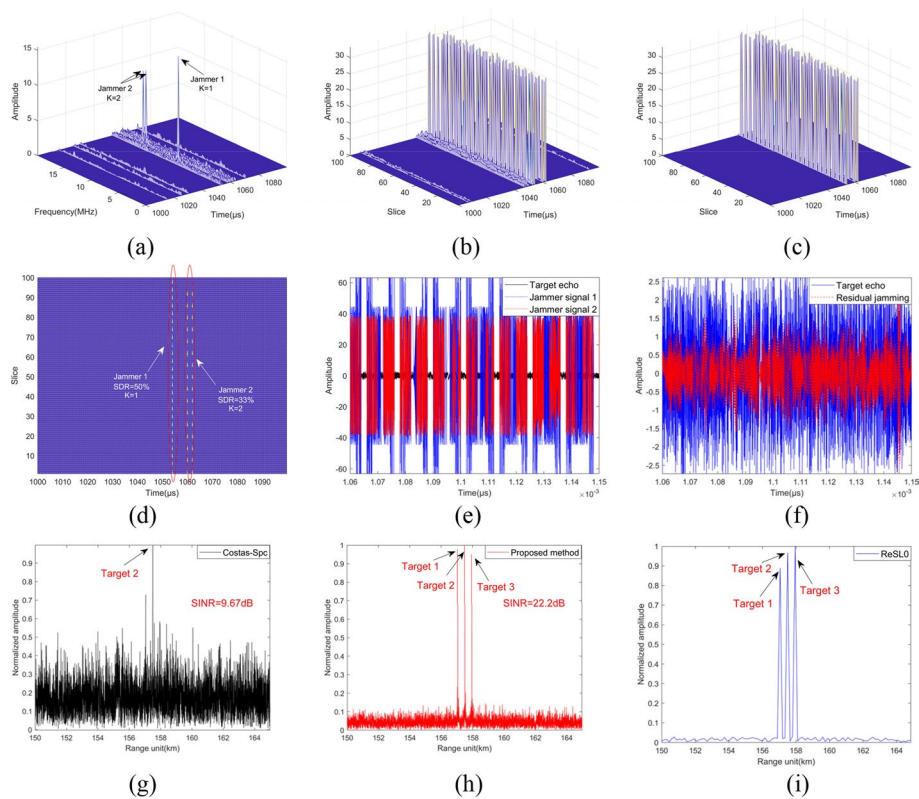

Fig. 9 Experiment results of scenario 1. **a** Delay-frequency plane. **b** Delay-slice plane. **c** Jamming identification result. **d** Top view of Jamming identification result. **e** Received jamming signal. **f** Received jamming after cancellation. **g** PC result of Costas-SPC. **h** PC result of the proposed method. **i** Range dimension sparse recovery result

Ji *et al. EURASIP Journal on Advances in Signal Processing* (2024) 2024:55

Page 23 of 34

As shown in Fig. 9g and h, although both methods can accurately detect the target, the output signal interference-to-noise ratio (SINR) of the proposed method is significantly higher than the Costas-SPC method. This is because at least 50% of the transmitted signal segments are forwarded by the jammer, and the Costas-SPC method can only obtain at most 50% of the sub matched filter output for accumulation. In contrast, our method achieves effective stripping of jamming by accurately reconstructing the jamming waveform, thereby achieving higher pulse compression gain. Figure 9i shows the robust sparse recovery results in the distance domain, and it can be observed that the target peak is more prominent in this profile. Compared with Fig. 9h, this further facilitates the detection of real targets.

In scenario 2, as shown in Table 3, there are two jammers with different forwarding times, which causes the JDR and synthesized SDR to further increase. As shown in Fig. 10a, three jamming peaks appear on the delay-frequency plane: two peaks with the same frequency-shift are generated by jammer 2, and the other peak is generated by jammer 1. Figure 10b, c and d shows the recovered delay-slice plane and corresponding jamming identification result, respectively. It can be seen that the ISRJ generated by jammer 1 is located at the block with 1054 μs, and the duty ratio reaches 50% in this block. The ISRJ generated by jammer 2 is located on the blocks with delay of 1058 μs and 1060 μs, with a duty ratio of 33%. Since the signal slices forwarded twice are the same, the jamming pulse sequence numbers on these two blocks are also the same.

Figure 10e and f shows the jamming distribution before and after jamming cancellation, respectively, showing that the jamming energy before cancellation is much larger than the target signal, and most slices are covered by jamming. After the jamming is cancelled, the jamming intensity is reduced to a level comparable to the target echo.

Table 3 Parameters settings of scenario 2

Parameter	Value
Target 1	
Time-delay	1047 μs
SNR	−10 dB
Target 2	
Time-delay	1050 μs
SNR	−10 dB
Target 3	
Time-delay	1053 μs
SNR	−10 dB
Jammer 1	
Forwarding time	1
Modulation delay	2 μs
Modulation frequency	8 MHz
JNR	30 dB
Jammer 2	
Forwarding time	2
Modulation delay	8 μs
Modulation frequency	16 μs
Modulation sampling time	2 μs
JNR	20 dB

Ji *et al. EURASIP Journal on Advances in Signal Processing*   (2024) 2024:55

Page 24 of 34

Fig. 10 Experiment results of scenario 2. **a** Delay-frequency plane. **b** Delay-slice plane. **c** Jamming identification result. **d** Top view of Jamming identification result. **e** Received jamming signal. **f** Received jamming after cancellation. **g** PC result of Costas-SPC. **h** PC result of the proposed method. **i** Robust sparse recovery result

However, there is still a strong jamming residue near 1145 μs. This may be due to the large deviation in the estimation of the jamming slice intensity corresponding to this time-delay. Therefore, in the PC results in Fig. 10h, a small number of jamming harmonics appears near the targets. In comparison, the PC result of the Costas-SPC method in Fig. 10g is not ideal. Since most signal segments are intercepted by the jammer, the number of narrowband filters available for accumulation is reduced, making target 1 and target 3 unrecognizable in the noise. Figure 10i shows the robust sparse recovery result of scenario 2, where the three targets are more clearly visible. This is because although a small number of strong jamming slices remain after cancellation, the JDR is greatly reduced and the integrity of the jamming waveform is destroyed. Therefore, the residual jamming is difficult to match the range waveform atoms and cannot accumulate output at the specified position.

In the more extreme scenario 3, as shown in Table 4, there are two jammers with the forwarding time $K = 1$, and their sampling start times differ by one jammer sampling pulse width. As shown in Fig. 11e, in this case, the target echo is completely covered by the jamming, almost all signal segments are captured by the two jammers, and the synthesized SDR is close to 100%. As can be seen from Fig. 11a, b and c, even in this case, the parameters of the jamming can be accurately estimated, and the jamming slices can also be accurately identified in Fig. 11d. It is noteworthy that the two

Ji *et al. EURASIP Journal on Advances in Signal Processing*   (2024) 2024:55

Page 25 of 34

Table 4 Parameters settings of scenario 3

Parameter	Value
Target 1	
Time-delay	1047 μs
SNR	−10 dB
Target 2	
Time-delay	1050 μs
SNR	−10 dB
Target 3	
Time-delay	1053 μs
SNR	−10 dB
Jammer 1	
Forwarding time	1
Modulation delay	2 μs
Modulation frequency	8 MHz
JNR	20 dB
Jammer 2	
Forwarding time	1
Modulation delay	6 μs
Jammer sampling start time	2 μs
Modulation frequency	16 MHz
JNR	20 dB

columns of jamming slices recovered in Fig. 11d are staggered in order, which also demonstrates that all sub-pulses of the transmitted signal have been intercepted and forwarded by the two jammers. As shown in Fig. 11f, h and i, even after cancellation, the jamming intensity is still within the acceptable range, and the three targets can still be detected after PC or robust sparse recovery. In contrast, the narrowband filtered output of the Costas-SPC method is completely contaminated by jamming data, which is equivalent to all-pass filtering of the jamming. Figure 11g shows that since the jamming echo is modulated by frequency, the ISRJ PC output under the agile frequency waveform does not appear as a false target group similar to the real target, but presents an irregular, noise-like PC output, causing the target to completely indistinguishable. This verifies the effectiveness of the proposed method in complex scenarios with multiple targets, high JDR and high synthesized SDR.

4.3 Analysis of target detection performance

To investigate the effects of SNR and jammer-to-noise ratio (JNR) on target detection, we conducted a series of 1000 Monte Carlo simulations for each of the three distinct jamming conditions in the three scenarios. Through these comprehensive simulations, we were able to assess the effectiveness of jamming suppression by meticulously evaluating the target detection rate P_A. P_A represents the probability of successfully detecting the target on the PC profile or on the range domain recovery profile. A high detection rate indicates better jamming suppression performance. Furthermore, for the simple detector, we set a threshold that is half the square of the maximum value of the pulse compression results, which is 3dB lower than the maximum value of the PC results. For
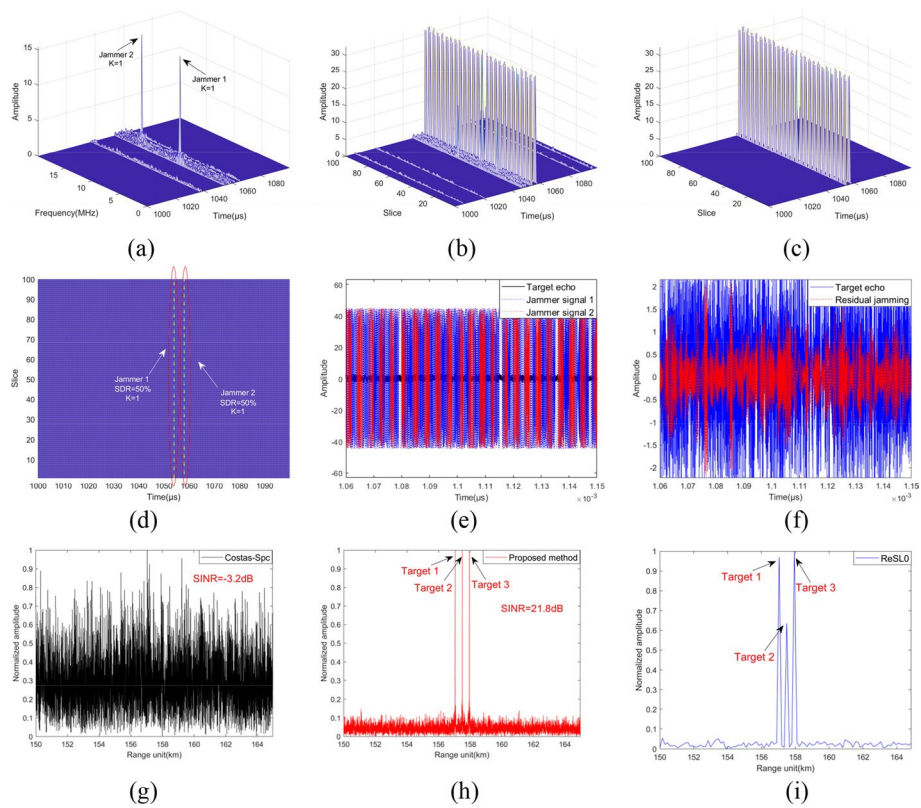
Fig. 11 Experiment results of scenario 3. **a** Delay-frequency plane. **b** Delay-slice plane. **c** Jamming identification result. **d** Top view of Jamming identification result. **e** Received jamming signal. **f** Received jamming after cancellation. **g** PC result of Costas-SPC. **h** PC result of the proposed method. **i** Range dimension sparse recovery result
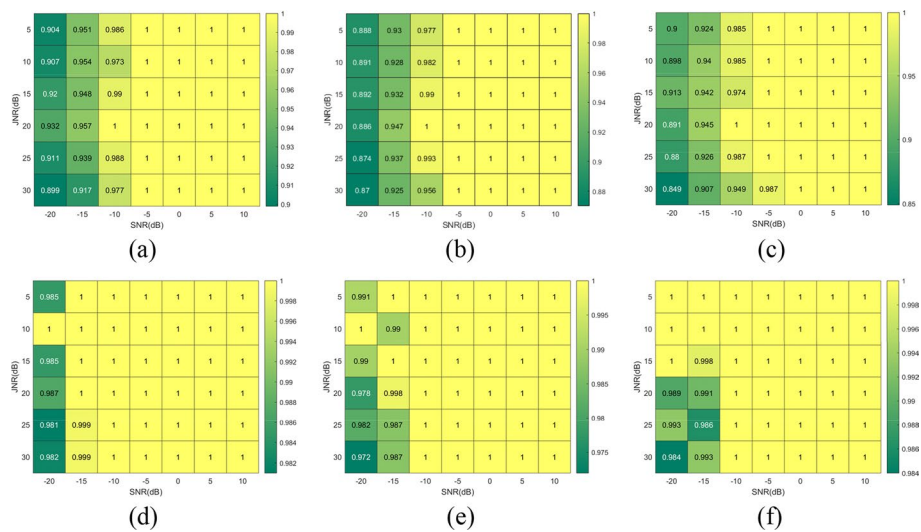

Fig. 12 P_A versus SNR and JSR. **a** Scenario 1, PC. **b** Scenario 2, PC. **c** Scenario 3, PC. **d** Scenario 1, robust sparse recovery. **e** Scenario 2, robust sparse recovery. **f** Scenario 3, robust sparse recovery

Ji *et al. EURASIP Journal on Advances in Signal Processing*   (2024) 2024:55

Page 27 of 34

the sparse recovery results in the range domain, this threshold is half the square of the maximum value of the recovery results. As shown in Fig. 12 we could see that:

(i) (i). In the analysis of PC results, when SNR ≥ -15 dB, the target detection rate P_A in the three scenarios stably exceeds 90%. Even under lower SNR conditions, P_A remains above 85%. The exceptional performance in this context can be attributed to the effective suppression of jamming, primarily dependent on the precise extraction of jamming parameters. A crucial element in ensuring this is maintaining a high JNR. In comparison to scenario 1, the augmentation in the number of jammers in scenario 2 and scenario 3 results in an increased number of jamming slices. This increase could potentially result in more robust residual jamming. Consequently, the target detection rate in scenario 2 and scenario 3 is marginally lower than that in scenario 1. Moreover, while the jamming encountered in scenario 3 is more intricate than in scenario 2, the target detection rates in both scenarios are comparable. This similarity arises from the distinct discernibility of the jamming slices when analyzed on the delay-slice plane.

(ii) In the analysis of range domain sparse recovery results, the radar's target detection capability remains remarkably stable, largely unaffected by increases in jamming intensity or enhancements in JDR and SDR. This stability arises because, even though in certain cases, like when some jamming sub-pulses are not fully detected or eliminated, jamming harmonics may be generated post pulse compression, the energy of most jamming slices is effectively suppressed. The residual jamming struggles to accumulate effectively on the sparse recovery's distance profile. Furthermore, the chosen method of sparse recovery is robust, demonstrating significant adaptability to low SNR. Therefore, target detection on the robust sparse recovery distance profile is more stable.

4.4 Analysis of parameters estimation performance

The estimation accuracy of parameters has a critical impact on the performance of the proposed method. As mentioned before, we focus on three jamming parameters: modulation delay, modulation frequency, and sub-pulse sequence number. Among them, although the estimation deviation of some sub-pulse sequence numbers may lead to inaccurate reconstruction of some sub-pulses in the jamming echo, this has a limited impact on the overall effect of jamming cancellation. However, errors in modulation frequency and modulation delay estimation will directly lead to a serious mismatch between the reconstructed jamming waveform and the actual waveform. This mismatch will significantly reduce the effect of jamming suppression. Therefore, we conducted a series of experiments under various JNR conditions to evaluate the estimation accuracy of these two parameters. Specifically, we conducted 1000 Monte Carlo simulations and assessed the parameter estimation accuracy by the probability of accurately recovering the modulation time delay and frequency-shift in these 1000 experiments.

As shown in Fig. 13, under the condition where JNR < 0 dB, the accuracy of parameter estimation is low, insufficient for accurate reconstruction of the jamming slices. However, when JNR reaches 0 or higher, the accuracy of estimating the jamming parameters
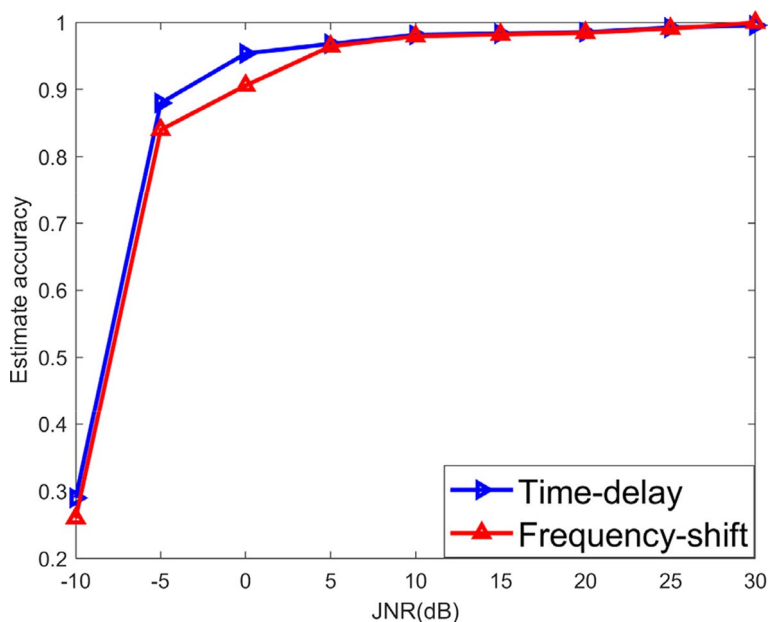
Fig. 13 Parameter estimation accuracy versus JNR

significantly improves, exceeding 90%, and approaches nearly 100% when JNR $\geq$ 5 dB. Considering that in practical scenarios the intensity of ISRJ is usually higher than the noise level, it can be inferred that the parameter estimation process is stable and reliable. Moreover, it is observed that at all JNR levels, the accuracy of estimating time-delay is consistently higher than that of frequency-shift. This phenomenon can be explained as follows: in the sparse recovery process of delay-frequency block model, the BOMP method first locates the time-delay blocks that may contain the jamming synthetic signal, and then further confirms the jamming frequency-shift within these potential blocks. Therefore, if the jamming time-delay blocks cannot be accurately located in the initial search phase, it becomes even more difficult to determine the exact frequency-shift of jamming.

4.4.1 Analysis of jamming suppression performance

In this section, we will first discuss the impact of sub-pulse width on jamming suppression effectiveness. The key to the proposed method lies in accurately identifying and reconstructing those sub-pulses that have been intercepted and modulated by the DRFM, in order to suppress jamming through a cancellation approach. An inappropriate choice of sub-pulse width may lead to insufficient or excessive reconstruction of the jamming echo, thereby causing significant residual jamming. Therefore, the selection of sub-pulse width is directly related to the performance of jamming suppression. To quantify the extent to which jamming is suppressed, we introduce the concept of the Interference cancellation ratio (ICR), which is defined as the ratio of jamming input power to jamming output power. The simulation results are shown in Fig. 14.

It can be seen from Fig. 14 that as JNR increases, the ICR shows an upward trend. Moreover, under different JNR levels, the proposed method can cancel the jamming
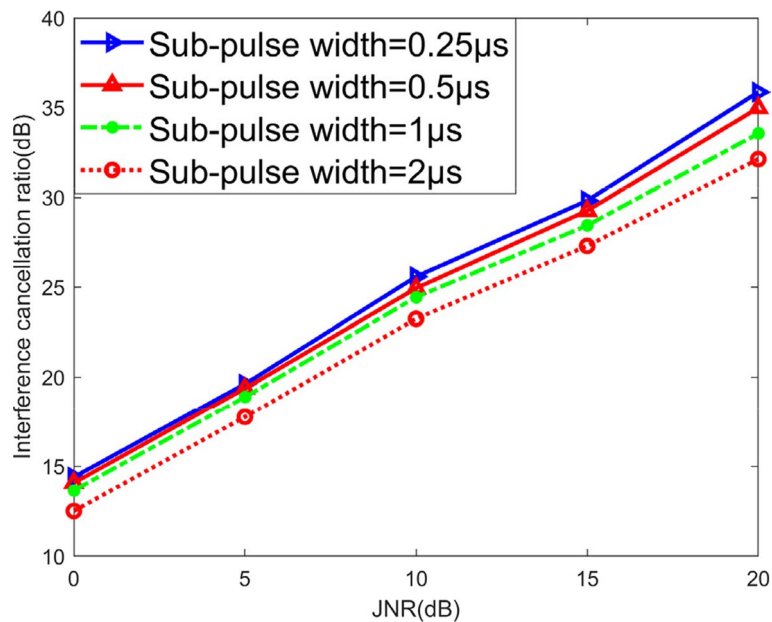
Fig. 14 ICR versus sub-pulse width

to a level similar to the target intensity, showing stable jamming suppression capability. In addition, as the sub-pulse width decreases, the characteristic difference between the reconstructed jamming and the real jamming in the sub-pulse dimension is reduced, and the fit to the real jamming is improved, which is reflected in a higher ICR. Especially for jammers with a sampling pulse width of 2 μs, setting the sub-pulse pulse width to 2μs is enough to effectively cancel most of the jamming slices. Therefore, in practical applications, the design of sub-pulse width should give priority to the sampling pulse width lower than that of the jammer to ensure efficient jamming suppression capabilities.

In our previous analysis, a key assumption was that the signal slices forwarded by the jammer contained one or several complete sub-pulses. However, in practical applications, due to potential delays in detection and sampling of radar signals by the jammer, the actual forwarded jamming slices may not match the predefined sub-pulses. To thoroughly investigate the impact of this mismatch on the effectiveness of jamming, we adjusted the sampling start time of the jammer and introduced sampling mismatch ratio (SMR) to quantify the degree of mismatch. Specifically, SMR is defined as the ratio of the misalignment length between the sub-pulse forwarded by the jammer and the original transmitted sub-pulse to the width of the sub-pulse. In Fig. 15, we analyzed the impact of different SMR on jamming suppression capability under the jamming parameters for Scenario 1. The results show that when the SMR is below 20%, the proposed method still maintains the ICR within an acceptable range. As the misalignment of the pulses increases, the mismatch between the reconstructed jamming and the real jamming intensifies, leading to an increase in residual jamming energy and a significant decline in the ICR. In such situations, using pulse compression for target identification is severely affected by the irregular peaks caused by residual jamming. As illustrated in Fig. 16,
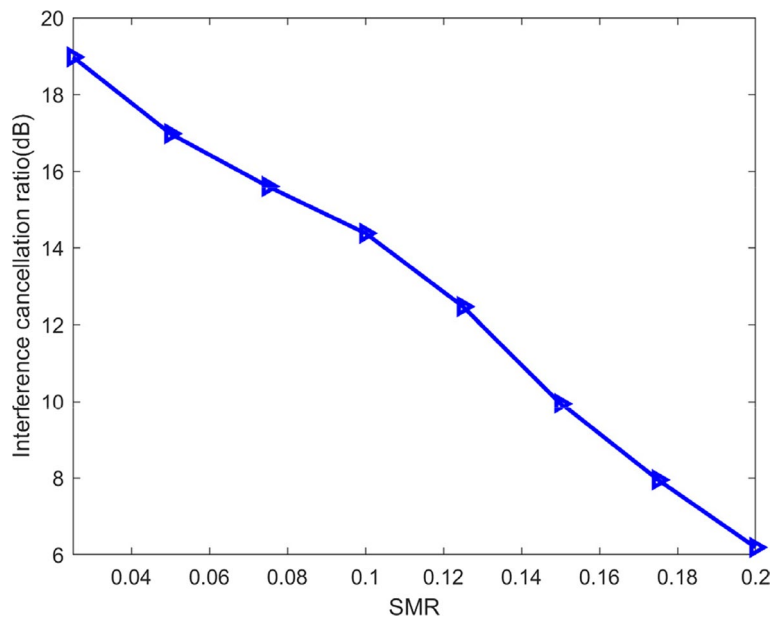
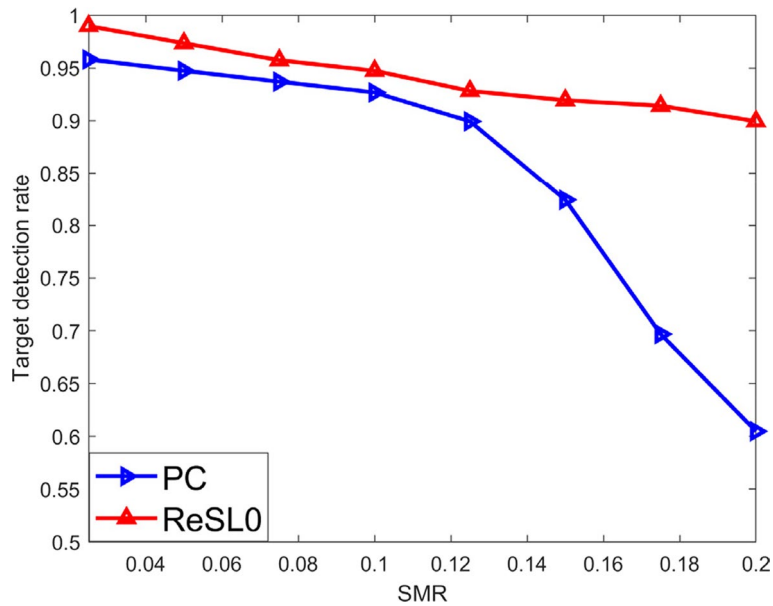**Fig. 15** Impact of incomplete interception on jamming suppression

Fig. 16 Impact of incomplete interception on target detection

although an increase in SMR reduces the ICR and decreases the target detection rate through pulse compression, the waveform difference between residual jamming and real target remains considerable. During the sparse recovery process, this can be considered as color noise. In the range profile obtained through robust recovery using the AReSl0, the target detection rate remains relatively high. It should be noted that the impact of incomplete interception can be further mitigated by reducing the sub-pulse width.
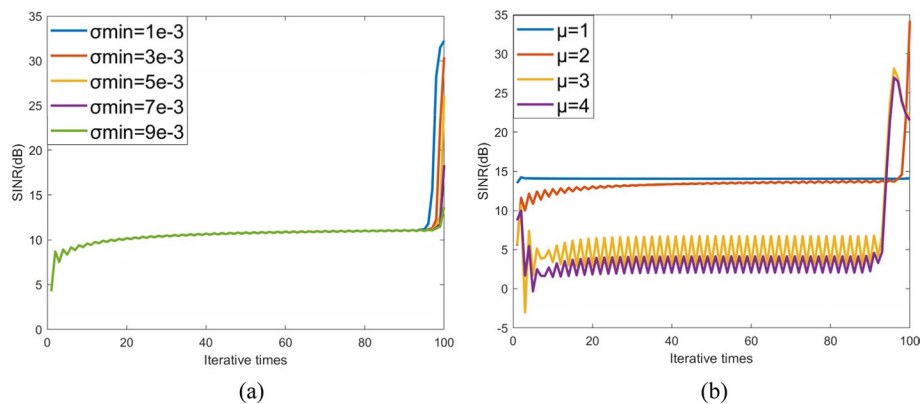
Fig. 17 Convergence curves of robust sparse recovery. **a** Different $\sigma_{\min}$. **b** Different μ

However, this approach may lead to an increase in the synthesized bandwidth, thereby raising the requirements for the radar's sampling frequency.

4.5 convergence experiments

In this section, we analyzed the convergence curves of the robust sparse recovery algorithm. We considered a scenario with a single target (SNR $= -10$ dB), while examining the impact of two key parameters: the final iteration value $\sigma_{\min}$ and the iteration step size μ, on the performance of the algorithm. Herein, we selected SINR as the vertical axis metric. Here, SINR represents the ratio of target power to noise power in the sparse recovery's range unit. Initially, we set different values of $\sigma_{\min}$ to assess the algorithm's convergence performance. Since $\sigma_{\min}$ directly influences the fitting degree of the objective function to the l_0 norm at the end of the outer loop, it is decisive for the algorithm's ultimate convergence accuracy. Figure 17a indicates that as $\sigma_{\min}$ decreases, the objective function can fit the l_0 norm more precisely, leading to an upward trend in SINR, reaching as high as 35 dB. Furthermore, under different $\sigma_{\min}$ values, the algorithm's convergence SINR significantly surpasses that of traditional pulse compression methods. It is noteworthy that there is a lower limit to reducing $\sigma_{\min}$, mainly for two reasons: firstly, if $\sigma_{\min}$ is too small, it may cause the objective function to be insufficiently smooth in the initial phase of the outer loop, leading to the final result falling into local optima; secondly, in our experiments, we found that the best recovery effect occurs when $\sigma_{\min}$ is reduced to 1 to 2 times the noise level. Further reduction would lead the algorithm to "learn" the noise values, deviating from the true solution, which aligns with the conclusion of Mohimani [35].

The choice of iteration step size μ also affects the algorithm's convergence behavior. Specifically, if μ is too large, the gradient solutions obtained in the early phase of the outer loop might skip the optimal solution interval, causing fluctuations in output SINR in the early iterations, as shown in Fig. 17b. This figure also reveals that the final SINR reaches its highest level at a certain $\mu = 2$. Moreover, we observed that the SINR of the last few iterations seems superior to that of the final iteration when μ takes other values, suggesting that the optimal $\sigma_{\min}$ may vary with different μ.

Ji *et al. EURASIP Journal on Advances in Signal Processing*   (2024) 2024:55

Page 32 of 34

5 Conclusion

This article presents a novel method for the suppression of ISRJ. Through a detailed analysis of ISRJ generation, we have developed two sparse models: the delay-frequency model and the delay-slice model. These models are capable of sparsely representing both targets and ISRJ. Targeting these models, we specifically designed a frequency-agile waveform that satisfies the RIP condition. Subsequently, we employed a block sparse recovery algorithm to identify ISRJ and estimate its three key parameters, thereby reconstructing the jamming slices to cancel ISRJ. Moreover, we introduced a new method based on robust sparse recovery that achieves more stable target identification compared to traditional PC. We have also optimized the method with an adaptive update mechanism for regularization parameters, enhancing its effectiveness and adaptability. Experimental results indicate that the proposed method can stably suppress ISRJ in various scenarios. Especially in scenarios with high JDR and high SDR, this method demonstrates stable anti-jamming capabilities and target detection abilities. However, the method currently faces limitations in addressing situations where there are changes in the frequency modulation of the jamming slices by the jammer, presenting a potential area for future research and improvement.

Abbreviations

ISRJ	Interrupted-sampling repeater jamming
PC	Pulse compression
LS	Least square
JDR	Jamming duty ratio
SDR	Sampling duty ratio
DRFM	Digital radio frequency memory
PRI	Pulse repetition period
LFM	Linear-frequency modulation
STFRFT	Short-time fractional Fourier transform
CFAR	Constant false alarm rate
FrFT	Fractional Fourier transform
RIP	Restricted Isometry Property
MIP	Mutual Incoherence Property
SINR	Interference-to-noise ratio
JNR	Jammer-to-noise Ratio
SMR	Sampling mismatch ratio

Ji *et al. EURASIP Journal on Advances in Signal Processing*   (2024) 2024:55

Page 33 of 34

References

1. L. Yan, P. Addabbo, C. Hao, D. Orlando, A. Farina, New ECCM techniques against noiselike and/or coherent inter-ferers. IEEE Trans. Aerosp. Electron. Syst. **56**, 1172–1188 (2019). https://doi.org/10.1109/TAES.2019.2929968
2. D. Orlando, A novel noise jamming detection algorithm for radar applications. IEEE Signal Process. Lett. **24**, 206–210 (2016).https://doi.org/10.1109/LSP.2016.2645793
3. D. Orlando, A novel noise jamming detection algorithm for radar applications. IEEE Signal Process. Lett. **24**, 206–210 (2016). https://doi.org/10.1109/TSP.2020.3047523
4. T. Tian, F. Zhou, X. Bai, Z. Zhang, B. Zhao, W. Fan, A partitioned deceptive jamming method against TOPSAR. IEEE Trans. Aerosp. Electron. Syst. **56**, 1538–1552 (2019). https://doi.org/10.1109/TAES.2019.2933958
5. C.P. Heagney, Digital radio frequency memory synthetic instrument enhancing US navy automated test equip-ment mission. IEEE Instrum. Meas. Mag. **21**, 41–63 (2018). https://doi.org/10.1109/MIM.2018.8423745
6. Y. Li, X. Jia, Y. Chen, C. Yin. Frequency agility MIMO-SAR imaging and anti-deception jamming performance. 2014 XXXIth URSI General Assembly and Scientific Symposium (URSI GASS), 2014. IEEE, 1–4. doi: https://doi.org/10.1109/URSIGASS.2014.6929631
7. N. Levanon, Stepped-frequency pulse-train radar signal. IEE Proc. Radar Sonar Navig. **149**, 297–309 (2002). https://doi.org/10.1049/ip-rsn:20020432
8. H. Qiongdan, L. Yong, C. Wei, L. Weihua, L. Bo. A new multicarrier chaotic phase coded stepped-frequency pulse train radar signal and its characteristic analysis. In: 2015 IEEE 10th Conference on Industrial Electronics and Applications (ICIEA), 2015. IEEE, 444–448. doi: https://doi.org/10.1109/ICIEA.2015.7334154
9. J. Chen, W. Wu, S. Xu, Z. Chen, J. Zou, Band pass filter design against interrupted-sampling repeater jamming based on time-frequency analysis. IET Radar Sonar Navig. **13**, 1646–1654 (2019). https://doi.org/10.1049/iet-rsn.2018.5658
10. W. Xiong, G. Zhang, W. Liu, Efficient filter design against interrupted sampling repeater jamming for wideband radar. EURASIP J. Adv. Signal Process. **2017**, 1–12 (2017). https://doi.org/10.1186/s13634-017-0446-3
11. C. Zhou, Q. Liu, X. Chen, Parameter estimation and suppression for DRFM-based interrupted sampling repeater jammer. IET Radar Sonar Navig. **12**, 56–63 (2018). https://doi.org/10.1049/iet-rsn.2017.0114
12. Y. Meng, L. Yu, Y. Wei, P. Tong. A novel parameter estimation method of interrupted sampling repeater jamming. In: 2019 IEEE International Conference on Signal, Information and Data Processing (ICSIDP), 2019. IEEE, 1–5. doi: https://doi.org/10.1109/ICSIDP47821.2019.9173164
13. J. Chen, X. Chen, H. Zhang, K. Zhang, Q. Liu, Suppression method for main-lobe interrupted sampling repeater jamming in distributed radar. IEEE Access **8**, 139255–139265 (2020). https://doi.org/10.1109/ACCESS.2020.3000278
14. B. Han, X. Qu, X. Yang, W. Li, Z. Zhang, DRFM-based repeater jamming reconstruction and cancellation method with accurate edge detection. Remote Sens. **15**, 1759 (2023). https://doi.org/10.3390/rs15071759
15. H. Yuan, C.-Y. Wang, X. Li, L. An, A method against interrupted-sampling repeater jamming based on energy function detection and band-pass filtering. Int. J. Antennas Propag. **2017**, 1–9 (2017). https://doi.org/10.1155/2017/6759169
16. J. Chen, S. Xu, J. Zou, Z. Chen, Interrupted-sampling repeater jamming suppression based on stacked bidirec-tional gated recurrent unit network and infinite training. IEEE Access **7**, 107428–107437 (2019). https://doi.org/10.1109/ACCESS.2019.2932793
17. W. Wu, J. Zou, J. Chen, S. Xu, Z. Chen, False-target recognition against interrupted-sampling repeater jamming based on integration decomposition. IEEE Trans. Aerosp. Electron. Syst. **57**, 2979–2991 (2021). https://doi.org/10.1109/TAES.2021.3068443
18. R. Shen, X. Liu, J. Sui, X. Wei. Study on interrupted-sampling repeater jamming performance based on intra-pulse frequency coded signal. Ninth International Conference on Digital Image Processing (ICDIP 2017), 2017. SPIE, 1012–1016. doi: https://doi.org/10.1117/12.2281779
19. H. Dai, Y. Zhao, H. Su, Z. Wang, Q. Bao, J. Pan, Research on an intra-pulse orthogonal waveform and methods resisting interrupted-sampling repeater jamming within the same frequency band. Remote Sens. **15**, 3673 (2023). https://doi.org/10.3390/rs15143673
20. C. Zhou, F. Liu, Q. Liu, An adaptive transmitting scheme for interrupted sampling repeater jamming suppression. Sensors **17**, 2480 (2017). https://doi.org/10.3390/s17112480
21. Z. Liu, Y. Quan, S. Du, Y. Wu, M. Sha, M. Xing, A novel ECCM scheme against interrupted-sampling repeater jam-ming using intra-pulse dual-parameter agile waveform. Digital Signal Process. **129**, 103652 (2022)
22. J. Zhang, H. Mu, S. Wen, Y. Li, H. Gao, Anti-intermittent sampling repeater jamming method based on LFM seg-mented pulse compression. J. Electron. Inf. Technol. **41**, 1712–1720 (2019). https://doi.org/10.11999/JEIT180851
23. J. Zhang, H. Mu, S. Wen, S. Liao, M. Sha, Anti-intermittent sampling jamming method based on intra-pulse LFM-Costas frequency stepping. Syst. Eng. Electron. **41**, 2170–2177 (2019)
24. L. Ding, R. Li, Y. Wang, L. Dai, F. Chen, Discrimination and identification between mainlobe repeater jamming and target echo by basis pursuit. IET Radar Sonar Navig. **11**, 11–20 (2017). https://doi.org/10.1049/iet-rsn.2015.0301
25. B. Zhou, K. Duan, W. Liu, R. Li, Y. Wang, Sparse Bayesian learning-based mainlobe blanket jamming suppression algorithm. J. Eng. **2019**, 7069–7073 (2019). https://doi.org/10.1049/joe.2019.0407
26. Y. Cheng, D. Zhu, J. Zhang, High precision sparse reconstruction scheme for multiple radar mainlobe jammings. Electronics **9**, 1224 (2020). https://doi.org/10.3390/electronics9081224
27. L. Yan, P. Addabbo, C. Hao, D. Orlando, J. Liu. A sparse learning approach to multiple noise-like jammers detec-tion. In: 2019 Photonics & Electromagnetics Research Symposium-Fall (PIERS-Fall), 2019. IEEE, 155–161. https://doi.org/10.1109/PIERS-Fall48861.2019.9021566
28. Wang, Z., Li, J., Yu, W., Luo, Y. & Yu, Z. 2022. A novel interrupted-sampling repeater jamming suppression method based on time-frequency analysis and target sparse reconstruction. *International Journal of Antennas and Propa-gation,* 2022. https://doi.org/10.1155/2022/2812456
29. R.G. Baraniuk, Compressive sensing [lecture notes]. IEEE Signal Process. Mag. **24**, 118–121 (2007). https://doi.org/10.1109/MSP.2007.4286571

30. K. Olivier, M. Gouws. Modern wideband DRFM architecture and real-time DSP capabilities for radar test and evaluation. In: 2013 Saudi International Electronics, Communications and Photonics Conference, 2013. IEEE, 1–4. https://doi.org/10.1109/SIECPC.2013.6551019

31. W. Ying, S. Changyong, Z. Shengjun, H. Peilin, J. Jinzu, Array ISAR of precessional cone target generated by intermittent sampling repeater jamming in fast and slow time. J. Electron. Inf. Technol. **38**, 450–454 (2016). https://doi.org/10.11999/JEIT150464

32. Y.C. Eldar, P. Kuppinger, H. Bolcskei, Block-sparse signals: Uncertainty relations and efficient recovery. IEEE Trans. Signal Process. **58**, 3042–3054 (2010). https://doi.org/10.1109/TSP.2010.2044837

33. J. Chen, Y. Zhou, L. Jin, J. Li, Y. Zhu, An adaptive regularized smoothed ℓ^0 norm algorithm for sparse signal recovery in noisy environments. Signal Process. **135**, 153–157 (2017). https://doi.org/10.1016/j.sigpro.2017.01.004

34. H. Bu, R. Tao, X. Bai, J. Zhao, Regularized smoothed $\ell0$ norm algorithm and its application to CS-based radar imaging. Signal Process. **122**, 115–122 (2016). https://doi.org/10.1016/j.sigpro.2015.11.024

35. G. H. Mohimani, M. Babaie-Zadeh, C. Jutten. Fast sparse representation based on smoothed $\ell 0$ norm. Independent Component Analysis and Signal Separation: 7th International Conference, ICA 2007, London, UK, September 9–12, 2007. Proceedings 7, 2007. Springer, 389–396.

Publisher's Note

Springer Nature remains neutral with regard to jurisdictional claims in published maps and institutional affiliations.